THESIS

INVESTIGATION ON HAFNIUM OXIDE MIXTURES FOR UV COATINGS FOR FUSION ENERGY APPLICATIONS

Submitted by

Maxwell Weiss

Department of Electrical and Computer Engineering

In partial fulfillment of the requirements

For the Degree of Master of Science

Colorado State University

Fort Collins, Colorado

Spring 2025

Master's Committee:

Advisor: Carmen Menoni

Jesse Wilson
Justin Sambur

ABSTRACT

INVESTIGATION ON HAFNIUM OXIDE MIXTURES FOR UV COATINGS FOR FUSION ENERGY APPLICATIONS

Metal oxide thin films play a crucial role in optical coatings for high power lasers. High laser damage resistance optical coatings find use in vacuum windows, mirrors, laser crystals, and harmonic generation crystals in high average and peak power lasers. The laser damage of multi-layer dielectric optical coatings is limited by that of the high index of refraction material, which is typically hafnium dioxide. Therefore, this work is focused on improving the laser damage performance of hafnium oxide by modifying the material's optical and structural properties through doping or mixing with other metal cations for applications in ultraviolet interference coatings for λ=355 nm. UV coatings capable of enduring billions of laser shots unscathed are pivotal to drivers for inertial confined fusion energy (IFE).

The laser-induced damage threshold (LIDT) of metal oxide thin films is constrained by various intrinsic and extrinsic factors, including crystallinity, fabrication method, and defect incorporation during processing. The implementation of high LIDT optical coatings is primarily limited by the ability to engineer amorphous oxide layers with controlled structural and optical properties. For UV lasers, amorphous dielectric coatings are multilayer stacks of alternating layers of HfO2 and SiO2. HfO_2 has a high index of refraction and a high band gap at λ=355 nn while SiO_2 has a low index of refraction, offering sufficient index contrast to engineer high reflector and anti-reflection coatings at λ=355 nm. To optimize LIDT, mixed amorphous oxide alloys offer a promising

research direction for UV high energy lasers for IFE.

This thesis investigates a variety of metal oxide mixture thin films as the high index material in anti-reflection coatings for λ=355 nm. Primarily, the optical properties, laser damage performance, amorphous morphology, and electronic state analysis of hafnium oxide mixtures with SiO_2 and Al_2O_3 are investigated. These mixtures are fabricated with the biased target deposition (BTD) technique which is entirely unexplored in the context of high LIDT interference coatings. Two-layer anti-reflection (AR) coatings were designed and fabricated by reactive biased target deposition (BTD) using mixtures of HfO_2 and SiO_2, HfO_2 and Al_2O_3, as the high index layer and SiO_2 as the low index layer. The laser damage response was assessed from 1-on-1 and S-on-1 tests from which the laser induced damage threshold (LIDT) fluence was determined. It is shown that in BTD 2-layer ARs using mixtures of $Hf_{1-y}Si_yO_x$ and $Hf_{1-y}Al_yO_x$ the 1-on-1 LIDT increases with respect to the HfO_2/SiO_2 AR. The BTD ARs have a density higher than electron beam evaporated (EBE) HfO_2/SiO_2 ARs but lower than ion beam sputtered (IBS) HfO_2/SiO_2 ARs. The 1-on-1 LIDT of the BTD ARs is slightly lower than that of electron beam evaporated (EBE) HfO_2/SiO_2 ARs and ion beam sputtered (IBS) HfO_2/SiO_2 ARs. While the 10^4-on-1 LIDT of EBE ARs was higher than that of either sputtering method. Substrate etching prior to deposition and UV conditioning increase the 1-on-1 LIDT of sputtered ARs. The S-on-1 LIDT of BTD ARs decreases by ~25% for S=10 and remains unchanged to S=10^4 laser shots, indicating no accumulation fatigue.

ACKNOWLEDGEMENTS

I would like to acknowledge my advisor, Carmen Menoni, for her support and funding in my graduate studies. I acknowledge Aaron Davenport for his consistent help answering my many questions. I would like to thank Samuel Castro Lucas, for teaching me the LANS deposition system, good discussions, and unfaltering positivity. Ela Jankowska, for her positivity and good advice. I would like to thank Vladimir Savichev, Alex Meadows, and Kyoshi Yamamoto for teaching me the fundamentals of working on the optical table. Other people who assisted me along the way, Emmet Randel, Ruth Osovsky, and Sangita Bhowmick. I acknowledge the entire team of graduate students in the Advanced Beam Laboratory for continued friendship and scientific support through my years at CSU. Thank you to the Enam Chowdhury and his graduate students for the interesting conversations at the conferences we attended. Of course, the majority of the thanks goes to my family, without your continued support I could not have made it to this point.

I would like to acknowledge the Analytical Resource Core at Colorado State University for their assistance in learning x-ray techniques, Research Resource ID (RRID: SCR_021758). As well, this work is supported by the U.S. Department of Energy (DOE), Office of Science, Fusion Energy Sciences, under Awards No. DE-SC0024882: IFE-STAR and DE-SC0023878.

TABLE OF CONTENTS

Chapter 1 Introduction

Oxide coatings have a pronounced role in the success of high-power laser facilities, enabling beam steering and preventing unwanted reflections from optical elements under extreme conditions. At NIF, the 1064nm Nd:Glass wavelength, 1ω, is converted to the third harmonic, (3ω, λ=355 nm), before striking the target. Furthermore, NIF laser operation is limited by the 3ω LIDT of the anti-reflection and high-reflection coatings on the final optics in the beamline [6]. It has been determined that NIF optics typically exhibit damage site growth at ~4 J/cm^2, but to achieve fusion ignition they must operate at a fluence of 8 J/cm^2 [68]. Therefore, the optics are often damaged which necessitates an intricate and expensive optics recycling loop. The disadvantage of damaged optics in a fusion energy facility such as NIF is the laser downtime caused by breaking vacuum to replace the optics [67]. In pursuit of a fusion pilot plant, amorphous oxides resilient to high 3ω fluence for giga-shot operation are required. Consequently, investigations into materials with higher UV, nanosecond LIDT has been a focus of the laser damage research community [6,7,9,11,20]. In this laser regime, materials with higher band gap typically demonstrate higher LIDT. Hence, the highest performing metal oxides are HfO_2, Al_2O_3, and SiO_2 which have an optical band gap of ~5.4eV, ~6.5eV, and ~7.5 eV respectively. Silica is often used as the low index layer in interference coatings and has a LIDT that is typically more than double that of the high index materials (i.e hafnia). Accordingly, most research is focused on the damage threshold of the high index layers as this is the performance limiting LIDT. Optical coating scientists often utilize high band gap and low refractive index (>5.5eV) materials as the high index layer to improve LIDT [8]. A consequence of using higher

band gap materials is the lower refractive index. A lower refractive index increases the number of layers required to reach spectral requirements and makes the coating more susceptible to nodule incorporation [6]. Mixtures of oxides allow for tailoring the refractive index. Mixture materials have been shown to improve LIDT, with performance improvements as high as 2-4x [5].

The principal interest of this thesis is the effect of mixing higher band gap materials into HfO_2 for the purpose of making 3ω anti-reflection coatings for laser drivers of fusion. Unique to this research, I present the first investigation into the laser damage properties of amorphous oxide mixtures sputtered by biased target ion beam deposition. I report that a biased target ion beam sputtered AR coating with $Hf_{0.2}Si_{0.8}O_x$ as the high index layer improves the 3ω laser damage resistance by a factor of 2x compared to HfO_2. Al_2O_3 is a candidate material for the high index layer in the 3ω coatings at NIF, which has the same index of refraction as $Hf_{0.2}Si_{0.8}O_x$ [6]. My LIDT result on $Hf_{0.2}Si_{0.8}O_x$ demonstrates that it is an equally high performing material to Al_2O_3 and should be considered as a candidate for the high index layer. Furthermore, this work adds to the literature regarding the role of fabrication method, annealing, crystallinity, and laser conditioning on the 3ω laser damage resistance. The multi-shot LIDT results show that electron beam evaporation is the best fabrication method for 3ω coatings for fusion lasers because it does not degrade in LIDT with increasing shot number like IBS coatings. I demonstrated that substrate conditioning by dry etching with Ar/O_2 plasma increases the laser damage threshold of anti-reflection coatings by ~2x. By utilizing a raster laser conditioning protocol, I demonstrated a ~1.5x increase in LIDT in HfO_2 and $HfSiO_x$ coatings fabricated by biased target ion beam deposition. My laser conditioning results on ion beam sputtered HfO_2 AR's corroborate previous reports that dense IBS materials do not significantly improve in LIDT with laser conditioning [45].

In this chapter, background information and a review of literature on amorphous metal oxides is presented. Section 1.1 provides context on the fabrication, properties, and structure of amorphous oxides as it pertains to mixture materials. Section 1.2 provides the motivation for LIDT research in the ultraviolet and a review of the literature. Section 1.3 defines the scope of this work.

1.1 Motivation

1.1.1 Laser Driven Inertial Confined Fusion Energy

Laser driven inertial confined fusion (ICF) is a promising source of carbon free energy [106]. To achieve fusion ignition, the energy of the fusion reaction must exceed the energy deposited on target. The mechanism of energy gain is the production of ~3.5MeV alpha particles which deposit more energy in the plasma, thereby increasing the rate of fusion reactions [120]. This process is known as alpha-heating. In 2022, the National Ignition Facility demonstrated fusion ignition for the first time, owing to the increase in laser energy from 1.9MJ to 2.05MJ [106].

First suggested in 1972, fusion ignition by laser driven inertial confined fusion has been pursued by Lawrence Livermore National Laboratory (LLNL), but numerous scientific obstacles have hindered success [121]. The principle of ICF is the rapid heating of a target exterior, known as the ablator, to compress the interior fuel, often a deuterium-tritium mixture, to fuse atomic nuclei [120]. Deuterium and tritium are used because they have the largest fusion cross section [120]. In the experiments which achieved fusion ignition, the indirect drive method was utilized. Indirect drive implies the laser energy strikes a high Z number hohlraum, which produces x-rays via the inverse bremsstrahlung process, depicted in figure 1.5 [106].

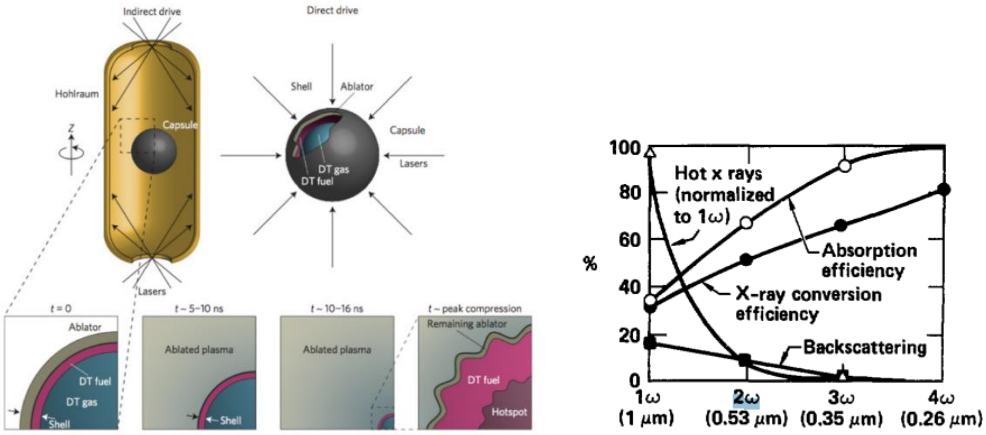

Figure 1.1 Diagram of indirect and direct drive ICF targets (left). Taken from [120]. Laser to plasma energy conversion percentage versus Nd:glass laser harmonic wavelengths (right). Taken from [132].

These x-rays heat the exterior ablator to plasma temperatures, starting the compression process. The laser wavelength is frequency converted to the third harmonic, 3ω, before striking the hohlraum. The benefit of 3ω over 1ω wavelength is increased laser to x-ray conversion efficiency, shown in figure 1.5 [132]. Longer infrared wavelengths strongly couple to Raman and Brillouin scattering processes and cannot penetrate dense plasmas, thereby decreasing the absorption by inverse bremsstrahlung [132].

The ability of plasma to start thermonuclear ignition is defined by the Lawson criteria, equation 1.9, where P the plasma pressure, τ is the compression time of the fuel, θ_α is the fraction of alpha particle energy deposited in the fuel and f(T) is a dimensionless parameter of temperature [122].

$$P\tau > 11 \cdot \frac{f(T)}{\theta_\alpha} \tag{1.9}$$

The Lawson parameter, P*τ, is essentially the primary value that needs to be maximized to achieve ignition. Interestingly, to increase the pressure a higher velocity plasma compression is needed, which subsequently reduces the compression time. Finding the balance between compression and Lawson parameters has proven to be a difficult

challenge inherent to laser driven ICF [106]. The pressure levels achievable with 2MJ of laser energy are on the order of giga-bars with temperatures of keV (1 keV->11 million C°). This extreme pressure creates ultra-high energy ions, which can overcome the massive Coulomb barrier required to fuse atoms [120]. The Lawson criteria was exceeded at NIF, by using 192 Nd:glass laser beams, frequency tripled to 351nm, delivering 2.05 MJ of UV laser energy on target.

1.1.2 National Ignition Facility (NIF) Laser for Fusion

A schematic depiction of the NIF laser used for fusion energy experiments is shown in figure 1.2, taken from [6]. The laser starts at the pre amp where a fiber optic laser with an energy of 200pJ is amplified by several stages to an energy of 6J using an Nd:glass regenerative amplifier. The wavelength entering the main amplifier is 1053nm, also referred to as 1ω [130]. This p-polarized pulse is injected into the transport spatial filter section and focused by the spatial filter SF3 into the main amplifier section. The seed pulse is amplified by five Nd:glass slabs before being injected into the main amplifier by way of reflection from LM3. At this time the Pockel cell changes the polarization of the beam such that it will be trapped in the laser cavity for 280ns. During this time the beam completes four passes through the main amplifier head which consists of 11 Nd:glass slabs. The Pockel cell changes the polarization causing the beam to leave the cavity and reflect from LM3. The beam is once again amplified by the power amplifier stage as it travels to the transport spatial filter. At this point, the infrared laser energy is on the order of 10^4 J, resulting in 3MJ of total energy between 192 beamlines. After reflecting from the transport mirrors, LM4-8, the beam arrives at the final optics assembly. In the final optics assembly, the beam is converted to the third harmonic by two potassium dihydrogen phosphate (KDP) optical crystals, 3ω, λ=351nm, with an efficiency of ~80% [132]. The 3ω beam is focused directly onto

the target using a wedged lens [132]. A fraction of the 1ω and 2ω energy remains in the beam which has undesirable effects on the x-ray conversion efficiency, figure 1.1[132]. To combat the effect of unwanted harmonics the 1ω and 2ω focus is placed far from the target to decrease the fluence.

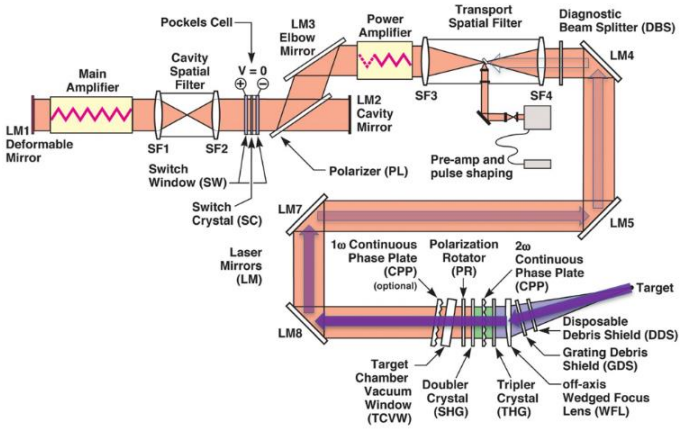

Figure 1.2 Schematic depiction of one of the 192 laser fusion drivers used by NIF to demonstrate fusion ignition. Purple arrow originating from the target represents backscattered 355nm light from the target. Taken from [6].

1.1.3 3ω Optics at NIF

Laser damage events occur most often in the final transport mirrors and final optics assembly. The final transport mirrors are HfO_2/SiO_2 multilayer dielectric coatings designed for high reflection (HR) at 1ω and anti-reflection (AR) at 3ω, figure 1.3 [6]. Anti-reflection at 3ω is necessary because 3ω light is backscattered from the target which increases the frequency of laser damage events, shown in figure 1.4 [6]. The final mirror, LM8, has a disproportionate frequency of damage events. This observation is explained by the ~90% transmission at each transport mirror, such that LM8 experiences the highest 3ω energy.

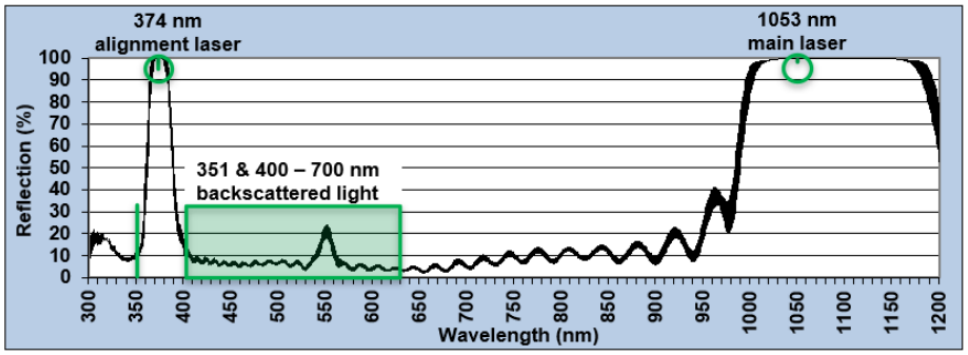

Figure 1.3 Spectral reflection of transport mirror LM8. Coatings are dichroic, designed for high reflection at 1ω (1053nm) and high transmission at 3ω (351nm).

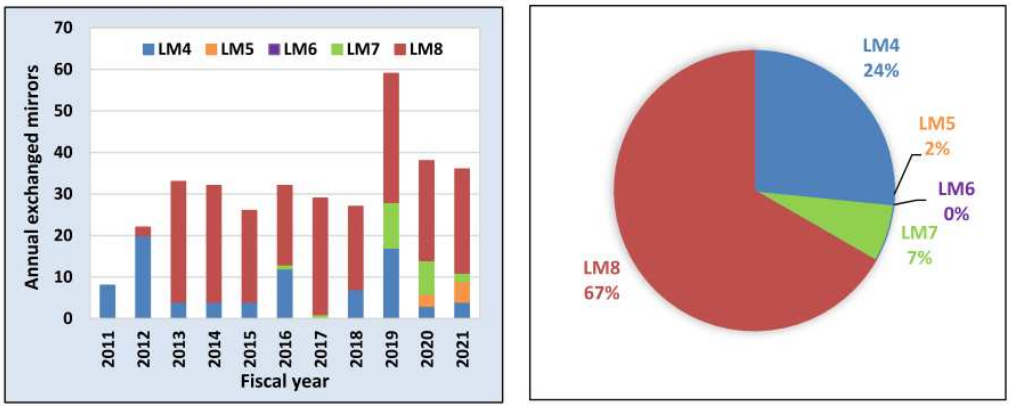

Figure 1.4 Annual number mirrors exchanged versus year (left). Relative frequency of damage events amongst dielectric "bouncing" mirrors LM4-LM8.
of backscattered light by Raman/Brillouin scattering

The KDP crystals and fused silica optics in the final optics assembly are anti-reflection coated using a porous silica single layer anti-reflection coating. The sol-gel AR coating uses near-spherical silica nanoparticles randomly oriented on the substrate surface. The thickness of the film is designed to provide ~99.5% transmission at 1ω and 3ω. Porous silica is used due to the high resistance of silica to laser damage [68]. Recent publications from Lawerence Livermore National Lab (LLNL) and the National Ignition Facility (NIF) indicate that the operating 3ω fluence incident on the final optics is as high 9 J/cm^2 [67]. Meanwhile, the empirically determined fluence at which damage sites grow in fused silica optics is 4 J/cm^{2,} illustrated in figure 1.6.

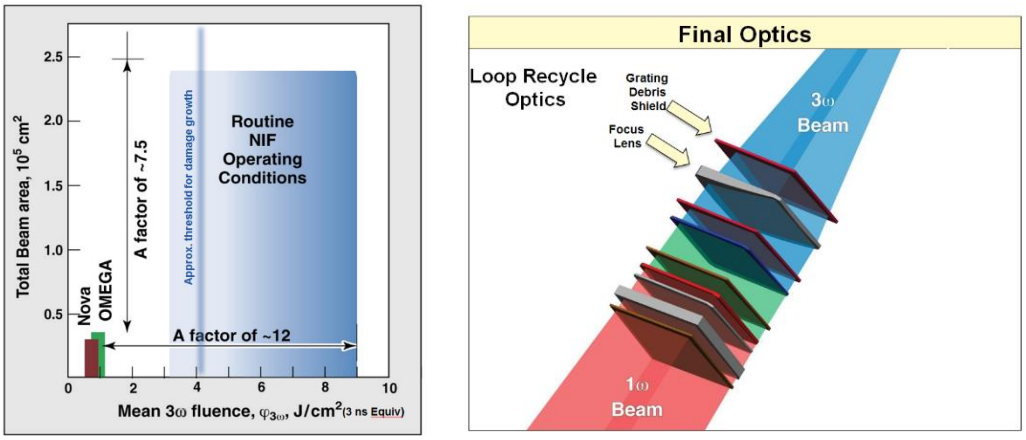

Figure 1.6) Laser beam area and operating fluences at the inertial confined fusion energy facilities, Nova, OMEGA, and NIF

NIF determined that optics could not be produced which are resilient to 3ω operating fluences higher than 4 J/cm^2 therefore the Optics Recycle Loop Program was established [68]. This program has several highly sophisticated process steps, all of which are necessitated by the low 3ω damage threshold of currently available optics. First is the *in situ* final optics damage inspection (FODI) which inspects each beam line from the target chamber. The FODI finds damage sites larger than 50um on final optics and tracks the growth of the damage sites during operation and determines when the optic needs to enter the recycle loop. Afterwards, damage sites which exceed an internally defined size threshold are ablated with a CO_2 laser in what they call the "damage mitigation" procedure [68]. The optic is then coated with a single layer porous silica anti-reflection coating deposited by sol-gel and post deposition treatment to create pores. After final inspection, the optic is inserted back into the beamline. This complex procedure illustrates the deficiency of laser damage resistant optics and the need for further research towards the improvement of 3ω LIDT. The operating fluence for 3ω coatings is defined by LLNL/NIF as a "functional damage threshold" where damage is defined as any laser-induced material change that can be detected in the performance

of the laser [72]. Ultimately, this indicates that the NIF has a higher tolerance for damage events.

1.1.4 Laser Damage Mechanisms in the Nanosecond Pulse Regime

Laser damage mechanisms can be divided into two categories, intrinsic and extrinsic. Intrinsic damage phenomenon can be elucidated by a combination of kinetic rate equations tracking electron density in the material's conduction band, n_e, shown in equation 1.10 [15].

$$\frac{\partial n_e(t)}{dt} = w_{pi}\big(I(t)\big) + w_{AV}\big(I(t)\big)n_e(t) + w_{defect}\big(I(t)\big)n_{defect}(t) - w_R(n_e(t), t) - w_{dr}(n_e, t) \quad (1.10)$$

The positive growth rate of conduction band electron density (units of $1/\text{cm}^3\text{s}$), w_{pi}, stems from the interaction between the laser field and the medium and is called the Keldysh multiphoton ionization model which depends on the intensity of the field [75]. This rate is pulse duration dependent. w_{av} is the avalanche ionization rate of free carriers, which is the dominant term in nanosecond pulse plasma generation (i.e ablation) [35].) While the negative rates, W_R and W_{dr}, is attributed to the relaxation of free carriers into the valence band as well as relaxation to defect levels. In the rate equation model, the defects are oxygen vacancy states. These mid gap defect states, allow for the UV laser radiation to be directly absorbed, accelerating electrons to energies beyond the avalanche ionization threshold. When electron energies are large, on the order of band gap of the material, the avalanche ionization rate in equation 1.10 becomes large

resulting in plasma formation. In UV laser damage, the role of oxygen vacancies as forbidden mid gap states is more pronounced due to the λ=355nm photon energy being larger than the deep vacancy energy in HfO_2, shown in figure 1.7 [1]. These oxygen vacancies can assist in the intrinsic damage process, as demonstrated by *Papernov et al* [1]. Once a critical density of electrons is produced, the second phase of the damage process begins on times scales much larger than the pulse length. In the final phase, melting or cracking occurs due to high temperature or high stress from the plasma shockwave [35].

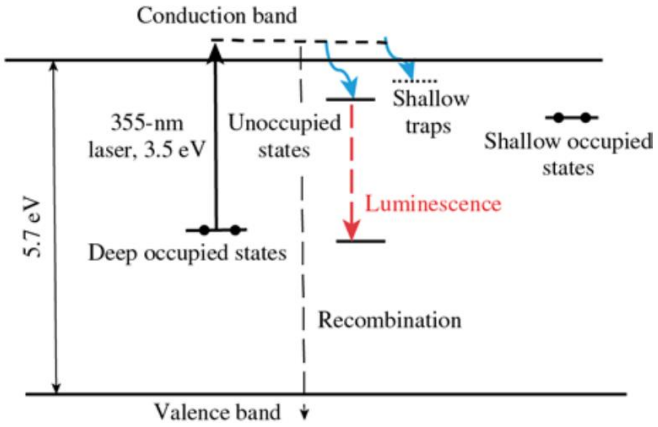

Figure 1.7 Energy band structure of HfO_2 with defect state levels depicted. Taken from [1].

In the nanosecond regime, extrinsic damage is a commonly observed damage mechanism, which is often called absorber-initiated [73]. The defect-initiated damage model is different from rate equation model, where the latter tracks the density of conduction band electrons and the former tracks the temperature of the material near a defect. In the rate equation model, the damage criteria is a critical electron density, while in the defect initiated model it is the melting temperature [35]. In the rate equation model, the oxygen vacancy defects

are assumed to be distributed evenly through the film, while the defect-initiated model focuses on the local thermal dynamics near an absorbing defect. The defect initiated thermal explosion (TE) model accurately predicts the square root pulse width scaling of laser damage threshold, shown in equation 1.11 and figure 1.8 where T_{cr} is critical temperature of the absorber, K_h is thermal conductivity of host, γ is the absorber absorptivity, and D is the effective absorber diffusivity, and F_{th} is the threshold fluence for damage [35].

$$F_{th} = \frac{T_{cr} K_h 8\sqrt{\tau}}{\gamma\sqrt{D}} \tag{1.11}$$

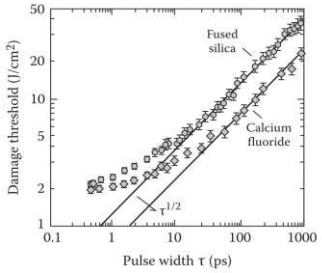

Figure 1.8) Pulse width dependence of damage threshold predicted by the TE model [35]. Note the departure from the square root law below 10 picoseconds.

In this model, a defect absorbs photon energies below the intrinsic band gap of the material. This absorber could be metal from the deposition chamber, cluster of oxygen deficient material, or another form of contamination. The parameters of the TE model are inclusion size, shape and the thermal and optical properties of the defect and host material.

1.1.5 Current Status of Research on Laser Damage of UV Coatings for High Power Lasers

Laser induced damage threshold (LIDT) is a measure of the highest fluence (J/cm^2) that a material can experience without having damage. The LIDT is dependent

on the type of laser damage test used. For example, the 1-on-1 LIDT measures the damage threshold when a single laser pulse is incident on a material. The S-on-1 test measures the damage threshold when multiple laser shots are incident on the material, typically S=10,100,1000, or 10000 shots. large area of the optic. Other types of tests exist, but the 1-on-1 LIDT demonstrates the fundamental damage threshold of the material. The details of these tests will be described in section 1.2.

The most common materials used in 355nm coatings are shown in figure 1.8, which illustrates the tradeoff between index of refraction and band gap. An optical coating is a combination of two layers of amorphous oxides with a contrast in refractive index. The low refractive index is typically SiO_2. For high laser damage coatings for 3ω, the most popular high index material is HfO_2, owing to its high band gap, (~5.4eV) and high index of refraction (2.2 @ 355nm). The majority of laser damage studies have focused on high index materials because these materials have lower laser damage resistance than the low index material. Figure 1.9 shows all high index materials submitted to the Boulder Laser Damage Symposium over 10 years of the competition [79]. Excluding hafnia, the only materials consistently considered for UV coatings are Al_2O_3 and a variety of fluoride materials, but primarily LaF_3 due to its index of refraction being higher than silica.

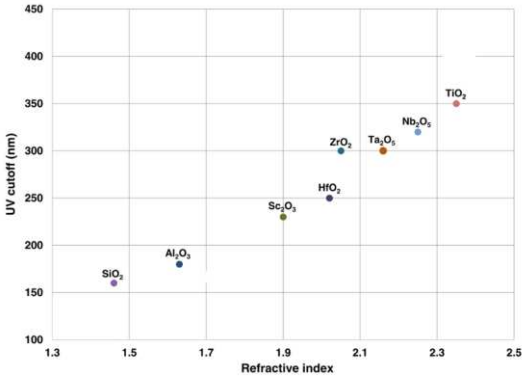

Figure 1.9.) Index of refraction vs UV cutoff wavelength for common materials used in optical coatings [79]

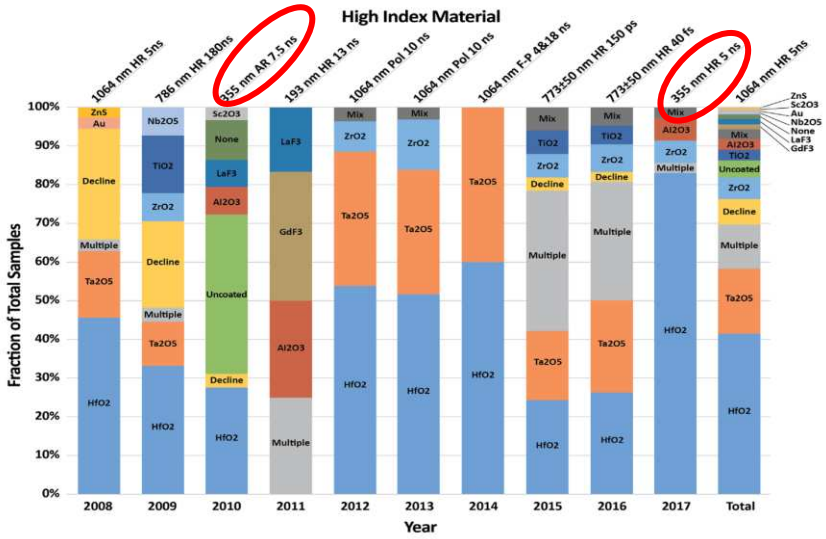

Figure 1.10.) High index materials submitted to the Boulder Laser Damage Symposium over the course of 10 years. Taken from [79]

Previous research has demonstrated the 1-on-1 3ω LIDT of HfO_2/SiO_2 high reflection (HR) coatings typically is in the range of 3-15 J/cm^2. NIF operates daily with a 355nm fluence of 8 J/cm^2, which is above the damage threshold of most HfO_2 based optical coatings. Several publications report an LIDT above the NIF operating fluence. First, *Jensen et al* 2010, reported an LIDT of 8.6 J/cm^2 for a 32-layer HfO_2/SiO_2 [11]. *Mende et al* measured a similar, ~7 J/cm^2 LIDT for an HfO_2/SiO_2 HR [88]. At the 2017 Boulder laser damage competition, HR coatings for 355nm were tested, and the results are shown in figure. 1.11. The HR coatings containing HfO_2/SiO_2 had a damage threshold in the range of 1 J/cm^2 to 12 J/cm^2.

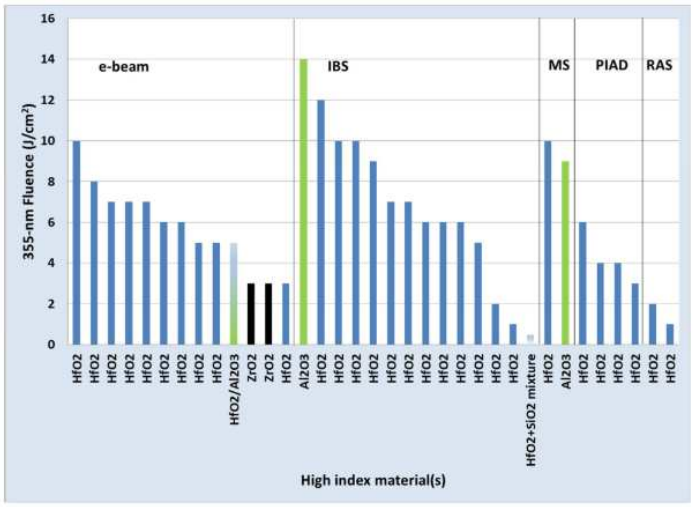

Figure 1.11.) 1-on-1 damage threshold of 355nm HR coatings submitted to the 2017 Laser Damage Competition. Taken from [79]

The 2010 Boulder laser damage competition tested the 355nm laser damage threshold of anti-reflection (AR) coatings, results shown in figure 1.12. The coatings were fabricated by many different companies and institutions. Therefore, these results illustrate the process-to-process variations that result in different LIDT for the same materials. The worst performing multilayer AR coating containing HfO_2/SiO_2 had a damage threshold of ~4 J/cm^2 and the best performing AR had a damage threshold of ~17 J/cm^2.

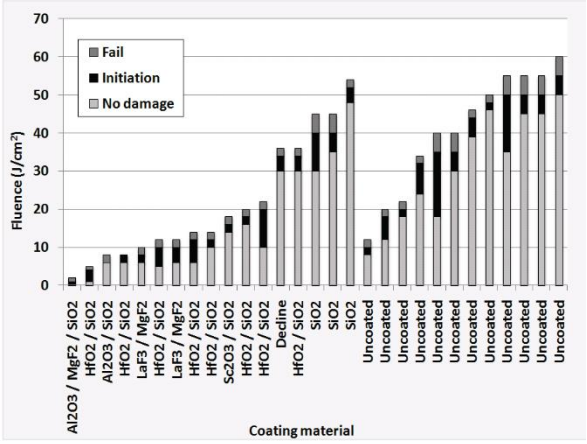

Figure 1.12.) 1-on-1 damage threshold of AR coatings submitted to the 2010 Laser Damage Competition. Taken from [79]

Several publications have reported different trends of 1-on-1 LIDT with HfO_2 mixture concentration when fabricated by PVD. Many of the observed trends agree, and many are in conflict. First, *Jensen et al* 2010 reports relatively weak correlation between band gap (i.e SiO_2 concentration) and 1-on-1 LIDT for single layers, (~4.2-6.5J/cm^2), with moderate SiO_2 concentrations performing better than high SiO_2 concentration mixtures, albeit within the error bars of each data point [11]. Simultaneously, the HR coatings of the same work observed a strong correlation with mixing and LIDT (8.6 -14.8 J/cm^2), below the 50% HfO_2 mixture level [39]. This is supported by *Mende et al* 2011 which reports a similarly large increase (>1.5x) in LIDT of HR coatings containing $Hf_{0.64}Si_{0.36}O_x$ and a $Hf_{0.63}Al_{0.37}O_x$ over pure HfO_2 [88]. Considering the role of polishing contamination at the surface demonstrated by *Abromavicius et al,* it is possible that single layer LIDT results are heavily impacted by the substrate [123]. This would explain why the high reflection coatings demonstrate a band gap scaling because the field strength is low at the substrate of a HR, while the opposite is true for single layers and AR's. Overall, the accumulated history of these results portrays a complicated image of the 3ω LIDT trend with dopant mixture concentration, illustrating the need for more comprehensive data on HfO_2 based mixtures.

1.2 Amorphous Thin Films

1.2.1 Structure, Properties, and Fabrication of amorphous thin films

Amorphous metal oxides are disordered materials that lack a long-range order [80]. Amorphous oxides are transparent at wavelengths from ~200nm to 3μm.

Amorphous metal oxides commonly used in optical coatings are characterized by an optical band gap transparency region with band gaps that vary from 3.5eV (TiO_2) to ~7.5eV (SiO_2). These materials have a small population of oxygen defects and other imperfections that manifest in the energy of the transmission edge. This is the so called Urbach tail" near the band edge [109]. However, oxygen vacancies and defect states can exist which allow for forbidden-gap transitions to occur, see figure 1.7 page 17 [1].

Amorphous oxides are often produced in physical vapor deposition (PVD) processes. They can also be produced by chemical vapor processes, such as atomic layer deposition [113]. An application of amorphous oxides is the preferential use of amorphous hafnium oxide in transistor gate oxides. This illustrates the principal benefit of its analogous amorphous oxide, which is there are no grains which are susceptible to defect incorporation.

Thin film metal oxides used in optical coatings are fabricated by PVD methods. These include electron beam vapor deposition (EBE), magnetron sputtering (MS), and ion beam sputtering (IBS). These techniques are used to create large area, isotropic films with excellent substrate adhesion which satisfies the requirements of optical coatings for fusion energy. Moreover, PVD techniques can deposit thin films on any type of substrate.

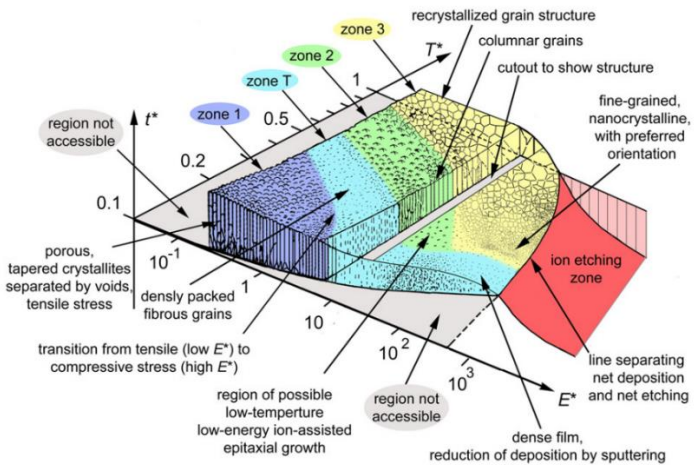

Figure 1.13 Structure zone model from [86], E is the adatom energy, T is the substrate temperature during deposition, and t is the thickness of the film

In this thesis, a slight variation on IBS, known as biased target deposition (BTD) or biased target sputtering (BTS), was used [85]. Each deposition method has a unique nano-scale morphology and atomic density, owing to the energy of the sputtered or evaporated material, known as adatom energy, and the temperature of the substrate during nucleation. In the well-known structure zone model of *Anders et al,* shown in figure 1.13, BTD and IBS films would fall into zone T, where the characteristic traits are compressive stress, high packing density, and an amorphous structure [86]. The specific differences between sputtering techniques will be discussed in section 2.1. Laser damage results of this thesis compare EBE to BTD and IBS, thus it is important to note that EBE processes have a lower adatom energy and subsequently fall into zone 1 of the structure zone model. EBE films often have a tensile stress, low density, and a vertically connected porous structure, which causes a low effective index of refraction [9]. This morphology will prove to be relevant to the LIDT results presented in chapter 3.

1.2.2 Dielectric Mixtures

Generally speaking, mixing material A into material B causes the new mixed material to take on the properties of A as the concentration of A increases, as depicted in figure 1.14 [78,19]. The properties of mixtures mostly follow this rule, but exceptions exist where the mixed material exhibits unique properties not observed in the pure materials [91]. For example, ferroelectricity is observed in Yttrium and hafnia mixtures at specific mixture percentages when annealed to a cubic phase and operated at cryogenic temperatures [117].

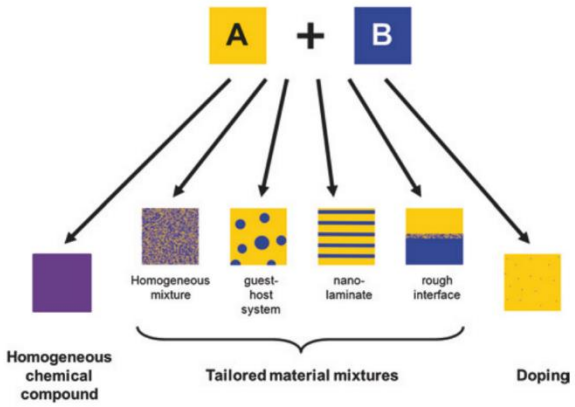

Figure 1.14 Classifications of mixtures found in optical materials. Taken from [19].

Reactively co-sputtered “mixtures” are a composite, which, unlike crystalline materials lack a complete coordination. For example, instead of a Hf-O-Si bond lattice there are also O-Hf-O and O-Si-O bonds in the network. These materials are macroscopically a homogenous mixture, where different bonding types exist locally at the atomic scale [80]. Despite a locally varying chemical structure, the long-range bulk optical and mechanical properties are homogenous and isotropic.

The bulk optical properties of mixtures are governed by the effective medium approximation, used to calculate the optical constants at varying mixture concentrations. The index of refraction versus mixture concentration is not a weighted

linear sum. In mixtures, one must consider not only the field in the host material, but the total electric field which includes the field created by the dopant dipole, E_{dipole} [31].

$$E_{actual} = E - E_{dipole} \tag{1.1}$$

$$E_{dipole} = -\frac{(N \cdot e \cdot r_e)}{3 \cdot \varepsilon_0} \tag{1.2}$$

$$q_e \cdot r_e = \alpha \cdot E_{actual} \tag{1.3}$$

Where N is the atomic density of dopants, $q_e * r_e$ is the dipole moment, α is the molecular polarizability, and ε_0 is the permittivity of free space. The polarization of the material is defined below, where x, is the susceptibility.

$$P = N \cdot q_e \cdot r_e = \varepsilon_0 \cdot \chi \cdot E \tag{1.4}$$

Combining equations 1.1-1.4 results in the following expression for the total index of refraction knowing that $x=n^2-1$.

$$\frac{(n^2-1)}{(n^2+2)} = 3\left(\frac{N\alpha}{\varepsilon_0}\right) \tag{1.5}$$

Equation 1.5 is commonly referred to as the Clausius-Mossotti relation, but modern literature calls this the Lorentz-Lorenz effective medium approximation (LL EMA) [77]. The more commonly used form of the LL EMA is shown in equation 1.6, where n_{eff} is the effective index of the mixture, n_1 is the index of material 1, n_2 is the index of material 2, f_1 is the volume fraction of material 1, and f_2 is the volume fraction of material 2.

$$\frac{\left(n_{eff}^2-1\right)}{\left(n_{eff}^2+2\right)} = f_1\frac{\left(n_1^2-1\right)}{\left(n_1^2+2\right)} + f_2\frac{\left(n_2^2-1\right)}{\left(n_2^2-1\right)} \quad (1.6)$$

The LL EMA is useful in calculating the mixture concentration of a thin film under test given a measured refractive index, n_{eff}, and a known index for materials n_1 and n_2. If the first material is the bulk metal oxide, n_{bulk}, and the second is air/vacuum with n_2=1,the following equation, 1.7, for the porosity of the film is created [21].

$$P(\%) = \left[1 - \frac{\left(n_{eff}^2-1\right)}{\left(n_{bulk}^2+2\right)}\right] \cdot 100 \quad (1.7)$$

The porosity, P(%), is the volume fraction of voids in the film, which is the ratio of f_1 to f_2. Utilizing equation 1.7 requires knowledge of the bulk index of refraction, n_{bulk}. The bulk index of refraction is taken from the literature and represents the index of refraction of the most highly dense form of the material, usually in the form of a crystal [77].

The other property of dielectric mixtures relevant to this work is the band gap. The band gap of dielectric mixtures scales approximately linear with mixture percentage as depicted in figure 1.15.

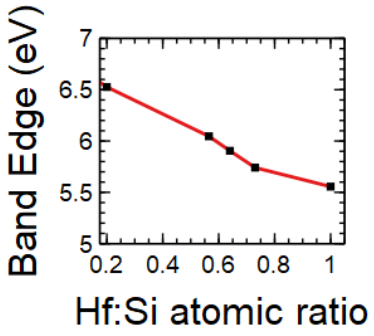

Figure 1.15 Band edge versus atomic ratio of Hf:Si in thin films fabricated by sputtering. Band edge is defined as the photon energy where transmittance falls to 80%. Hf:Si atomic ratio was measured by Rutherford Backscattering (RBS)

1.2.3 Metal Oxide Mixtures in Optical Coatings

Optical coatings are stacks of alternating dielectric materials with high and low index of refraction. Often referred to as Bragg mirrors, interference coatings, or multi-layer dielectrics, these devices are used to reflect, transmit, change polarization, or filter wavelengths from a light source. The layer thicknesses and refractive indices are chosen such that reflection from each interface constructively or destructively interfere in the reflected field. The simplest interference coating is the single layer, 0-degree angle of incidence (AOI), anti-reflection coating, where the film has a lower index of refraction than the substrate [19]. Complete destructive interference of the reflections will occur when the film thickness, t, and film refractive index, n_1, satisfies equation 1.8 and 1.11, where λ is the wavelength of interest, k_1 is the wavenumber in material 1, n_s is the index of the substrate, and n_1 is the index of the thin film. When the thickness of the film satisfies equations 1.8 the analytical expression for reflection of a single layer film in air, equation 1.9, reduces to equation 1.10 [115]. When equation 1.11 is satisfied R equals 0.

$$t = \frac{\lambda}{4n_1} \tag{1.8}$$

$$R = \frac{n_1^2(1-n_s)^2\cos^2(k_1 t)+(n_s-n_1^2)\sin^2(k_1 t)}{n_1^2(1+n_s)^2\cos^2(k_1 t)+\left(n_s+n_1^2\right)^2\sin^2(k_1 t)} \tag{1.9}$$

$$R = \frac{\left(n_s-n_1^2\right)^2}{\left(n_s+n_1^2\right)^2} \tag{1.10}$$

$$n_1 = \sqrt{n_s} \tag{1.11}$$

Equation 1.8 is the criteria for a quarter wave optical thickness (QWOT) layer. This AR design is used by NIF in the AR coating final optics [67]. An index of refraction smaller than the SiO_2 substrate is accomplished using a porous layer of SiO_2 which has a refractive index that satisfies equation 1.9 for n_s=1.45 [67].

The simplest high reflection (HR) coating design is the QWOT g(HL)^{x}a design, where g is the glass substrate, a is air, HL indicates a QWOT high/low index layer pair, and x is the number of layer pairs, depicted in figure 1.16. High reflection is achieved by tailoring the layers to satisfy equation 1.8, which causes constructive interference between the reflections from all interfaces. As you increase the number of layer pairs, the spectral bandwidth and reflection percentage increases, shown in figure 1.17 [115].

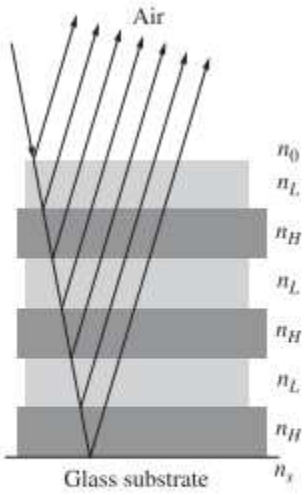

Figure 1.16 Illustration of the quarter wave mirror stack design- g(HL)^{3}a.

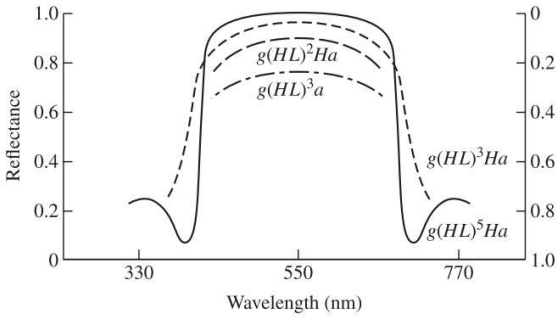

Figure 1.17 Reflectance (left) and Transmittance (right) of g(HL)^{x}a multi-layer dielectric HR coating with different structures. Taken from [115].

Engineers have utilized alternative HR designs that incorporate metal oxide mixtures to increase laser damage resistance. For example, using the Refractive Index Step Down (RISED) concept, figure 1.18 [88].

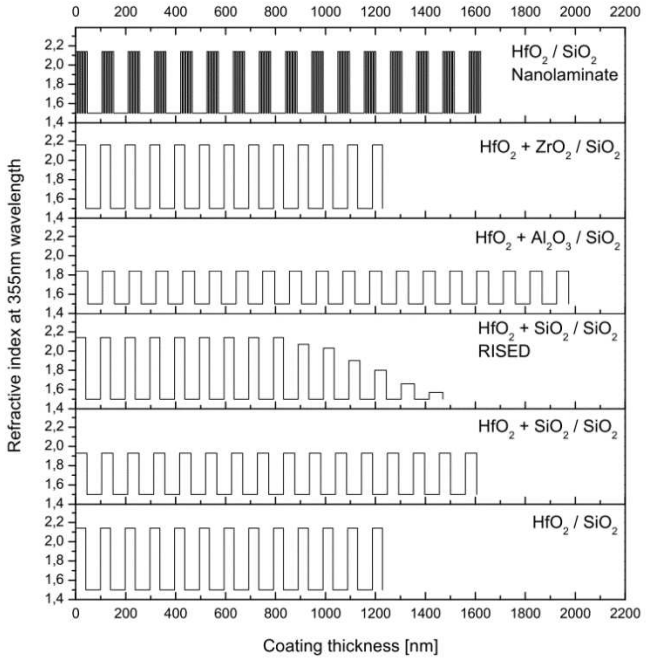

Figure 1.18 HR coating designs with different mixed oxide materials. Refractive index is the vertical axis while position in the coating is the horizontal axis Lower index materials require more layers (HfO2+SiO2)/SiO2, while RISED design requires fewer. Taken from [88].

The RISED principle is predicated on the band gap dependence of LIDT, the increased field strength at the surface of HR coatings, and the decrease in reflectance when using low refractive index mixtures [116]. Using low refractive index HfSiOx material throughout the HR stack would necessitate an increase in the number of layers, depicted in figure 1.18. By only using low refractive index mixtures in the high field strength layers at the surface one improves the laser damage resistance without sacrificing the thickness of the stack. The initial high index layers use an extremely low Hf concentration $HfSiO_x$ mixture (i.e high band gap) with increasing refractive index deeper in the stack.

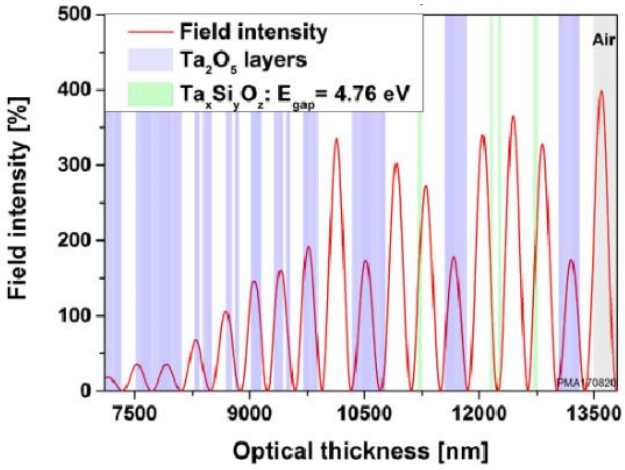

Figure 1.19 HR coating design of a Ta_2O_5 and $Ta_xSi_yO_z$ optimized design. The white is the SiO_2 layers. The high band gap mixture is placed in positions with high electric field strength. Taken from [14]

An alternative use of high band gap mixtures is shown in figure 1.19 [14]. In optical coatings with complex design requirements, mixtures are placed in the layers with highest standing wave field strength, which has the highest probability of laser damage [116]. At relatively low field strengths in the stack the lower band gap material is used. This design principle is similar to RISED, in that the goal is to improve LIDT without increasing the coating thickness.

1.3 Scope of the Work

In this thesis, I investigated material mixing of amorphous oxides by reactive co-sputtering methods. I characterized the optical and structural properties of these mixtures as dopant concentration increases using x-ray diffraction (XRD), RBS, and UV-Infrared spectroscopy. Furthermore, with x-ray photoelectron spectroscopy (XPS), I found significant modifications to the bonding network of hafnia doped with silica or alumina. It was determined that significant contributions of O-Si-O and O-Hf-O bond types exist in a bulk $HfSiO_x$ film. The crystallization of mixtures was evaluated, and the concentration required to suppress the crystallization of hafnia was empirically

determined. Additionally, I demonstrated that hafnia silica mixtures can be annealed to higher temperatures without crystallizing. In conjunction with these results, the increase in band gap with annealing was characterized and is caused by the oxidation of oxygen vacancies in the amorphous matrix. Next, a systematic study of the laser damage resistance of these mixtures in single-shot and multi-shot pulse testing was performed. For comparison, coatings fabricated by IBS and EBE were LIDT tested. This study elucidated the key mechanisms underpinning the LIDT of mixture coatings. For example, identifying Argon content in sputtered coatings revealed a mechanism by which sputtered coatings damage. Through precision LIDT testing I correlated the mixture concentration, band gap, annealing, and fabrication method to the laser damage resistance. Afterward, a unique laser conditioning experiment revealed the advantage of laser conditioning on the LIDT of hafnia-based coatings. Finally, an ensemble of tests was performed to determine the role of the substrate in the laser damage of AR coatings.

Chapter 2 Experimental Method

The amorphous oxides in this work are synthesized by ion beam sputtering and biased target deposition. These techniques provide thin films with high density, excellent uniformity, and easy control over mixture concentration which is all necessary for fusion laser coatings. Ion beam sputtering utilizes a gridded ion source which accelerates ions into a target to produce a vapor plume, while biased target deposition uses a voltage applied to the target to accelerate ions. We utilized biased target co-sputtering of multiple targets to produce amorphous oxides mixtures. Meanwhile, the ion beam sputtering system was used to produce binary films of HfO_2 and SiO_2. Section 2.1 provides a detailed description of the ion beam sputtering deposition systems used to grow the oxide thin films.

To extract information about the band gap and refractive index of sputtered mixtures ellipsometry and spectrophotometry were chosen as optical characterization tools. As well, spectrophotometry was necessary to measure the transmission spectrum of AR and HR coatings designed for this experiment. To ensure the films are amorphous and determine the crystallization temperature of mixtures glancing incidence x-ray diffraction was utilized. X-ray photoelectron spectroscopy was used to characterize the chemical bonding states and ensure sub-stoichiometric bonds are not present. Section 2.2 describes the thin film characterization techniques in more detail.

To determine the threshold at which an optical coating has a 0% probability of damage the ISO-21254-1 laser induced damage threshold test was performed. Additionally, multi-pulse laser damage tests were used to extract information about a coatings longevity under repeated 3ω laser pulses. To determine if laser conditioning has an effect on laser damage resistance a raster scan protocol was utilized. Section 2.3

describes the setup for measuring laser induced damage threshold and statistics used for damage threshold determination.

2.1 Ion Beam Sputtering Deposition

2.1.1 Biased Target Ion Beam Sputtering

Biased target deposition (BTD), sometimes referred to as biased target sputtering (BTS), is a sputtering process in which the sputter plume is generated by ions striking a negatively biased metal target [85]. In the BTD technique, low energy Ar ions are created by a Kauffman type end-Hall ion source [102]. The ground sheath is ~1mm away from the edge of the circular metal target which results in an electric field that is normal to the target far from the ground sheath. The Ar ions are attracted by the electric field from the voltage biased metal target [85]. A plasma sheath of Ar ions accumulates ~1cm from the surface of the metal target. Despite the plasma sheath, the ions gain kinetic energy equal to $e*V_{bias}$, where e is the charge of an electron [85]. The plasma sheath does not affect the final kinetic energy because electric fields resulting from the voltage applied to the metal target are a conservative field [115]. In this work the argon plasma pressure is 10^{-4} Torr during deposition. The use of argon as a process gas results in a minimal <5% concentration of argon in the deposited thin films. The voltage bias is pulsed between positive and negative at kHz frequency. The positive and negative bias prevent charge from accumulating on the target, which is the "target poisoning" phenomena. Target poisoning occurs when oxygen is backfilled into the chamber and reacts with the target to form an oxide layer on the metal target surface. If a DC bias is applied to the "poisoned" target charged argon will accumulate on the surface, until the electric field across the oxide exceeds the breakdown field, resulting in an arc event which can eject a cluster of material [96]. In this work V_{bias} is 800-900V, which

represents a high sputtering energy, and consequently causes a high energy of sputtered atoms (i.e adatoms) [87]. Typical adatom energy for PVD processes range from <1eV to as high at 10-15eV [13]. PVD processes with high adatom energy typically have high density and a packed structure with spherical voids at the nanoscale [9, 86]. The packed structure prevents ambient humidity from affecting the film, but in the context of nanosecond LIDT this structure may not necessarily be beneficial compared to a porous structure [9].

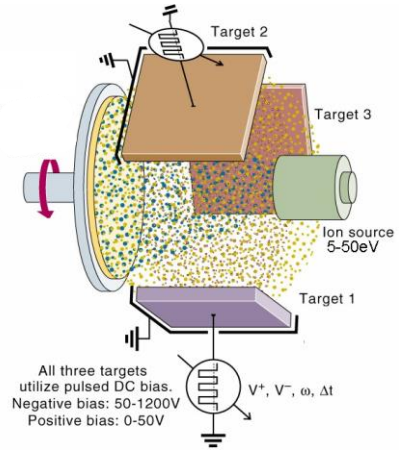

Figure 2.1) LANS system geometry and illustration of the principles of biased target reactive sputtering

The design of the commercial 4Wave Laboratory Alloy Nanolayer System (LANS) allows for 6 targets to be mounted at the same time in a hexagonal fixture, shown in figure 2.1. The use of a 3-channel pulsed voltage supply allows for independent control of the sputtering power applied to each target, and subsequently alloy concentration. The substrate is centered in the middle of the target fixture with a horizontal offset. The film uniformity is increased by rotating the substrate stage at 20 rpm. The first advantage of BTD is the ability to deposit on several substrates at the same time. Second, the deposition rate is slow, ~0.01nm/s, which allows for precision control of layer thickness. Third, and most importantly, is simple fabrication of mixture films,

without complex target assemblies often needed in IBS systems. The drawback of low deposition rate is the inability to make thick coatings >1μm.

2.1.2 Gridded Ion Beam Sputtering

Gridded IBS is among the most popular deposition technologies used in commercial optical coatings due to its high uniformity, fast deposition rate, dense film morphology, and stable deposition conditions. In this method a metal or dielectric target is sputtered using an argon ion beam with an energy exceeding 1keV. The argon plasma is generated in a confined space using 13MHz RF applied to a inductor coil. A series of metallic plates with holes, called grids, has high voltages applied which accelerates the argon plasma towards the target. The grids also have a spherical geometry which focuses the ion beam to a smaller size at the metal target. This is different than the BTD method, where a voltage applied to the metal target creates an electric field that accelerates ions to the target. In the IBS case, the argon ions are accelerated in a "ion beam", and must be aimed at the target. The use of argon as a process gas results in argon incorporation in IBS films as high as 0.5-0.7% atomic concentration. Researchers have shown this argon incorporation results in decreased laser damage resistance with nanosecond pulses [97]. Oxide formation occurs when oxygen is backfilled into the chamber directed at the target, with flow rates in the range of 10-50sccm. In this work, HfO2 and SiO2 are sputtered at 1.25keV, with 600mA argon beam current and 13sccm of O2 directed at the target. The deposition rate was ~0.16/0.22 nm/s respectively. The substrate stage was spun during deposition at a rate of 0.4 rotations per second in a planetary motion pattern.

2.2 Thin Film Characterization

2.2.1 Ellipsometry and Spectrophotometry

The measurement of optical constants was performed using optical techniques known as ellipsometry and spectrophotometry. Ellipsometry is a polarization spectroscopy technique that exploits the angle anisotropy between S and P polarized Fresnel coefficients to determine the dispersion of refractive index in a thin film under test. The ellipsometric spectrum is collected by illuminating the coating with a polarized white light source in a reflection geometry and collecting the reflection with a crossed polarizer and fiber. The intensity of the reflection is measured with S and P polarized light and sent to a spectrometer to select a specific wavelength. The ellipsometer in this work was the HORIBA UVISEL system. The ellipsometric equation 2.1 for the ellipsometric angles, Δ and ψ, is shown below. Δ and tan(ψ) represent the phase change and amplitude ratio between S and P polarizations.

$$\rho = \frac{r_p}{r_s} = \tan(\psi)\, e^{i\Delta} \tag{2.1}$$

Where r_p and r_s are the complex field reflection coefficients of the coating stack and is the aggregate of reflection from multiple interfaces. The ellipsometric spectra were measured at 60-degree angle of incidence (AOI) with a wavelength range of 190nm-1500nm. The data are modelled with commercial ellipsometry software to obtain the index refraction and thickness of a single thin layer of a specific material. The ellipsometer software, Delta2Psi, provides the framework for setting initial conditions, such as the number of layers in the coating, desired refractive index dispersion model, and predicted film thickness. The index of refraction models are physically significant and, in this work, a three oscillator Tauc modified Lorentz model is used [109]. The Tauc Lorentz is a variation on the classical Lorentz oscillator which models light-matter interactions as an electron mass on a spring representing the Coulomb force [31,115].

A simple Cauchy model is utilized for silica layers. The Levenberg-Marquardt data fitting algorithm then searches for oscillator coefficients until the index of refraction and thickness of the layers produces an ellipsometric spectrum that matches the measurements.

The next step in determining the optical constants of a thin film is measuring the transmission vs wavelength by UV-Visible spectrophotometry. The commercial spectrophotometer was a Perkin Elmer Lambda 1050. The transmission spectrum of a single layer on a glass substrate produces a so called "interference pattern" (i.e. oscillations in wavelength) that can be calculated by tracking the phase and amplitude of the reflected electric field due to each interface the coating stack [19]. Under the assumptions of a thick infinite substrate and an isotropic thin film the transmission spectrum has the analytical form shown in equation 2.2 [19].

$$T = \frac{\left(t_{12}^2 t_{23}^2 \frac{(n_3 \cos(\varphi_3))}{(n_1 \cos(\varphi))}\right)}{1+r_{12}^2 r_{23}^2+2r_{12}r_{23}\cos(2\delta)} \tag{2.2}$$

$$2\delta = 4\pi \upsilon d \sqrt{n_2^2 - \sin^2(\varphi)} = j\pi \tag{2.3}$$

Where t_{xy}/r_{xy} is the Fresnel amplitude transmission coefficient for light in medium x entering medium y, 2δ is the double pass accumulated phase in the layer, j is an integer number for the order of transmission maxima, n_1 is index of the entrance medium, n_3 is the index of the substrate, n_2 is the index of the thin film, d is the film thickness, φ is the angle of incidence, and υ is the optical frequency. Maxima occur when equation 2.3 is satisfied. That is, when 2δ equals an integer of pi, which corresponds to a QWOT, and at these wavelengths the transmission is identical to the substrate. Minima occur if the film thickness is half wave optical thickness (HWOT). An example of single layer spectra is shown in figure 2.2.

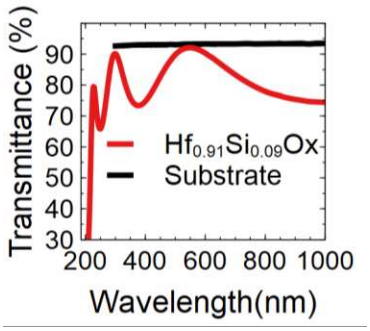

Figure 2.2) UV-Vis transmission spectra of a single layer of HfSiOx on UVFS

For this work, the optical constants and layer thickness determined by ellipsometry are loaded into a commercial optical coating software Optilayer™ and refined to match the measured transmission spectrum. In a similar fashion to ellipsometric data fitting, a Cauchy-Urbach model for the complex refractive index is fit to match the measured transmission data. The results of measurements made on the sample in figure 2.2 are shown in figure 2.3.

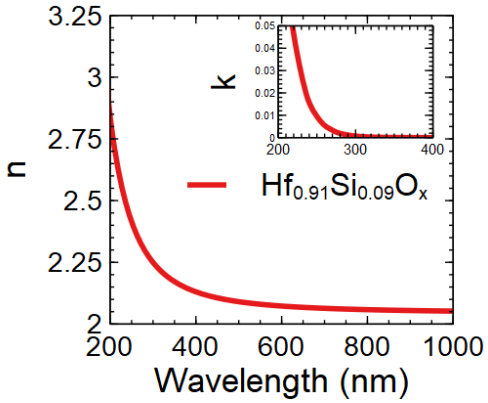

Figure 2.2) Reverse engineered refractive index of HfSiOx on UVFS, k is the complex part of the refractive index

2.2.2 X-ray Photoelectron Spectroscopy (XPS)

XPS is a technique used to identify atomic bonding in a material by measuring the energy of electrons liberated from the inner shells of atoms by absorption of high energy x-ray radiation [57]. It is important to note that electrons only escape from a shallow ~10nm depth on the surface of a sample, hence XPS is considered a surface

analysis technique. Information about the oxidation state and bonding environment are the key information gleaned from XPS. The energy of escaping electrons is measured by a hemispherical electron energy analyzer. Subsequently, the binding energy is calculated by conservation of energy balance, equation 2.3, where E_{photon} is the x-ray photon energy, $E_{kinetic/binding}$ is the kinetic/binding energy of the electron, and Φ is the work function of the detector. Φ is a known constant which is varies from system to system.

$$E_{binding} = E_{photon} - (E_{kinetic} + \Phi) \quad 2.3$$

The electron energy is characteristic of the atom and orbital from which it originated (i.e oxygen atom- 1s orbital). Emission lines from all atomic species are best described by Voigt functions, which is a convolution of a Gaussian and a Lorentzian line shape. The Lorentzian contribution is due to the natural Heisenberg uncertainty in the binding energy of bonded electrons. While the Gaussian is due to broadening processes that emitted electrons encounter as they escape the sample, such as phonon broadening [58]. In the data fitting of this thesis a 30% Gaussian lineshape function was used according to the recommendation of [58]. Analysis of the atomic percentages and bonding environment was performed on several hafnium silicate mixtures by XPS. To perform atomic concentration analysis the relative sensitivity factors (RSF) of each peak, inherent to the XPS system, were utilized to correct the measured counts per second. The differing RSF between core level electrons is due to differing photoionization cross sections.

The thin film samples analyzed were deposited onto Si substrates to reduce charging effects during measurement. High resolution spectra of the Hf 4f, Si 2p, and O 1s orbitals were obtained. XPS spectra was collected using the Physical Electronics PE 5800 ESCA/ASE spectrometer with monochromatic Al Kα X-rays (1486.6 eV) and a

take-off angle of 45°. A charge neutralizer was used during measurement with a 20uA electron current. The base pressure was 1×10^{-9} Torr, and 1×10^{-8} Torr during measurement. Analysis was assisted by CasaXPS software. Binding energy calibration was performed by deconvolving the C 1s peak with the C-C component attuned to the well-known energy of 248.8eV [65]. Atomic concentration was determined by integrating the appropriate metal peak and the relative sensitivity factor (RSF) of the emission.

2.2.3 Glancing Incidence X-ray Diffraction (GI-XRD)

X-ray diffraction is a technique used to measure periodic atomic structures in materials. When periodic atomic layers, found in crystalline structures, exist the conditions of Bragg's law, equation 2.4, can be satisfied to produce constructive interference.

$$2d \sin(\theta) = n\lambda \tag{2.4}$$

Where d is the atomic spacing, θ is the angle of incidence, n is an integer, and λ is the x-ray wavelength. This implies that the intensity, width, and angle of diffraction peaks reveal information about crystallinity and crystal orientation. In GI-XRD, the x-ray source is incident at a grazing angle <1° to prevent the crystallinity of the substrate from influencing the measurement.

Crystallization in PVD films depends on the material, adatom energy, deposition rate, thickness, and deposition temperature. The material at the center of this thesis, HfO_2, is often polycrystalline when deposited by BTD, showing signs of crystallization in a monoclinic form. The low crystallization temperature of HfO_2 is related to its uniquely low free energy change associated with the crystallization of a single HfO_2 compound [111]. Low energy deposition techniques, like EBE, often produce polycrystalline HfO_2. BTD HfO_2 is poly-crystalline as deposited, but most materials sputtered by BTD are amorphous. In higher adatom energy processes, like IBS, HfO_2 is typically amorphous. Regardless of the deposition parameters the temperature of crystallization is empirically

related to the thickness of the film through the following relation from [22].

$$T_c = T_{ac} + (T_{melt} - T_{ac})e^{-\frac{d}{C}} \quad (2.5)$$

Where T_c is the crystallization temperature of the thin layer, T_{ac} is the crystallization temperature of the bulk amorphous film, T_{melt} is the melting temperature, d is the film thickness, and C is a data fitting parameter. It follows from equation 2.5 that ultrathin layers can suppress the formation of crystallization.

The experimental details of the measurements in this thesis are as follows. The system used was a Bruker D8 Series II which is equipped with Cu K-α x-ray source (1.54 Å). A 0.6mm source slit was utilized. Two theta detector scan was performed from 20° to 65°. To minimize the contribution of the substrate an amorphous UVFS substrate was chosen. In conjunction with the choice of substrate, the angle of incidence of x-rays was fixed to a glancing angle of 0.8°. The 0° angle was calibrated by finding the stage position at which the intensity falls to 50% of its maximum. Then, by sweeping the stage angle from –1 to 5, the peak intensity on the sensor indicates a 0° AOI. These steps are iterated several times until the calibration angle does not change with further iterations.

2.2.4 Scanning Transmission Electron Microscopy/ Electron Energy Loss Spectroscopy (STEM-EELS)

Electron microscopy is necessary when the image resolution desired is smaller than the diffraction limited resolution of optical microscopy [128]. In this imaging methodology, quasi-monoenergetic electrons are focused onto a sample using electromagnetic “electron optics.” The focused electron probe has a size of <1nm, which is scanned across the sample. A bright field (BF) image is formed by the electrons transmitted through the sample that are not scattered or scattered to low angles. Therefore, bright regions of a BF image correspond to lower atomic density. A dark field,

also known as high Z contrast or high angle annular dark field (HAADF), image can be formed using a detector in an ring around the transmitted electron beam, shown in figure 2.4 as the ADF detector. Heavier atomic species, i.e high Z number, will scatter electrons to higher angles. This produces an image opposite of the BF, where bright regions indicate high density or higher Z number atoms. Example HAADF and BF images taken at the same location in a sample are shown in figure 2.3.

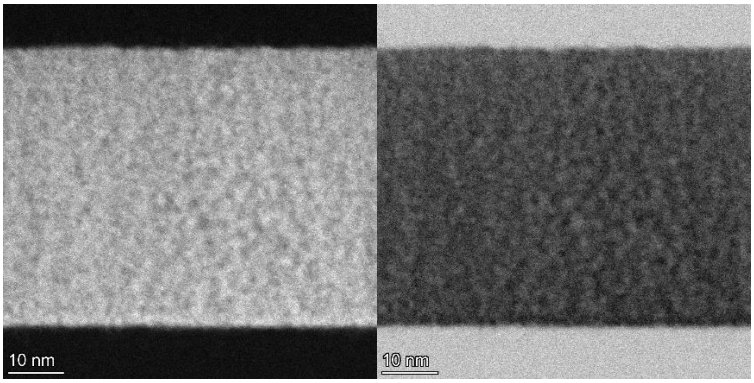

Figure 2.3) High angle annular dark field STEM image of HfSiOx (left) and bright field image of the same location (right).

Additionally, the STEM system arrangement shown in figure 2.3 allows for simultaneous electron energy loss spectroscopy (EELS). By measuring STEM images and EELS simultaneously spatial atomic mapping at the nanoscale is possible [128]. The physical principle of EELS relies on the assumption of a mono-energetic electron beam, typically on the order of 200keV. The probe electrons lose energy due to inelastic scattering which is measured by the electron spectrometer. Inelastic scattering is caused by several physical processes, but atomic fingerprinting is enabled by the known energy loss due to inner shell electron scattering. Each atomic species has characteristic inner shell electron transitions, for example, Hf atoms can be identified by the 1716eV ionization energy of M shell electrons [129].

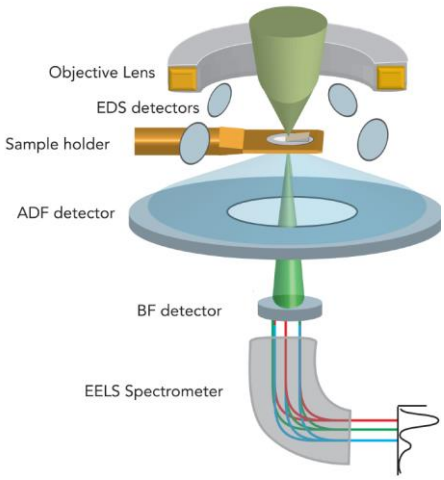

Figure 2.4) Simplified depiction of STEM-EELS experimental configuration. ADF=annular dark field, BF=Bright field

2.3 Laser Damage Testing

2.3.1 ISO-21254-1 Laser Damage Testing Setup

There are several different types of laser damage testing protocols, each provides a different type of information about the coating. The 1-on-1 damage test consists of using a single laser pulse to impinge on a single test site. The test involves shooting many (>10) test sites at a single laser fluence to calculate the probability of damage. The fluence is ramped from low to high such that a fluence was tested with 100% and 0% damage probability. An example of this test is shown in the microscope image, figure 2.5.

Figure 2.5) Nomarski microscope image at 5x magnification illustrating the result of a 1-on-1 LIDT test on an $HfSiO_x$ film. The high fluence rows are at the top, low fluence rows are at the bottom.

The probability of damage, P(F), at a fluence F, is determined by the fraction of test sites that incurred laser damage. In this work, 20 test sites were utilized at each fluence to get quality statistics. The only difference between the 1-on-1 test and the S-on-1 test is that S number of laser pulses are directed at each test site rather than a single pulse. Common S-on-1 test protocols are S=10,100,1000,or 10000 shots per test site. The damage probability is defined as in the 1-on-1 test. The goal of this damage test is to produce a single number for the laser induced damage threshold (LIDT) fluence that corresponds to P(F)=0. In this work, the LIDT is determined using the degenerate defect ensemble model [95]. The working principle of this model is that the laser beam with a gaussian fluence distribution is sampling the surface for defects. The defects are degenerate, meaning it is assumed that all defects damage at the same fluence, Tdefect. If the area of the laser beam with a fluence above Tdefect is coincident on a defect, a damage event occurs.

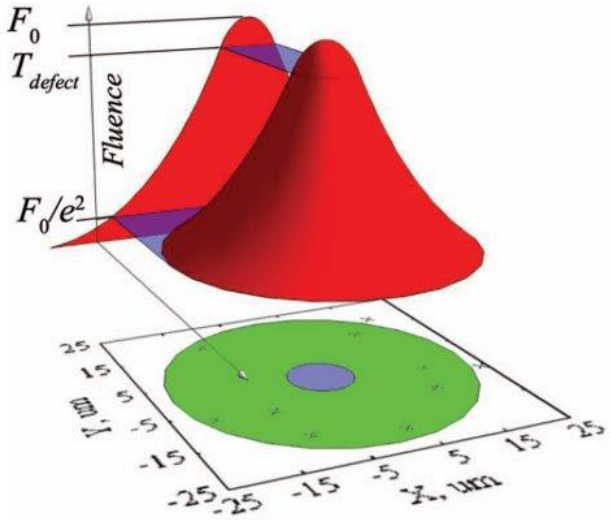

Figure 2.6) Visualization of the gaussian beam fluence distribution with a slice taken at the defect damage threshold, T_{defect}. F_0 is the peak fluence of the beam. The "x's" on the 2d projection represent a hypothetical distribution of defects on the surface. Taken from [95]

A useful visualization of the sampling characteristic of LIDT testing is shown in figure 2.6 [95]. Assuming a Gaussian fluence distribution given by equation 2.6, the area of the beam above the defect damage threshold, a, is given by equation 2.7, where w is the $1/e^2$ beam radii, r is the radial distance from the center of the beam, F_0 is the peak fluence of the beam. Assuming the defects are evenly distributed with an areal density, M, it follows that the expected number of defects within the significant area, a, is given by λ_d in equation 2.8 [98].

$$F(r) = F_0 e^{-\left(\frac{r}{\omega}\right)^2} \tag{2.6}$$

$$a\left(F_0, \omega, T_{defect}\right) = \pi\omega^2 \ln\left(\frac{F_0}{T_{defect}}\right) \tag{2.7}$$

$$\lambda_d = a \cdot M \tag{2.8}$$

Fundamentally, under the above assumptions, LIDT testing falls under the classification of a Poisson statistics problem because the probability of seeing x number of damage

events in a test site is determined by a constant mean rate, λ_d [124]. The Poisson distribution shown in equation 2.9, gives us the probability of d number of defects damaging in a single test site, Pr(d). However, LIDT testing is a binary system, a test site is either damaged, D, or not damaged, ND. Therefore, the probability of interest is P(D), the probability of at least one defect being damaged, shown in equation 2.10. The probability of not damaging is equivalent to the probability of 0 defects damaging. Combining equations 2.7, 2.8, and 2.10 gives us equation 2.11, the probability of damage at a fluence F. S is the $1/e^2$ beam area. Equation 2.11 is fit to the experimental laser damage data with a weighted least square regression, shown in figure 2.5. The regression fits the defect density and the defect damage threshold, which is the LIDT. A heavier weight is given to the fluences with a probability greater than 0%. The dotted lines shown are the 95% confidence interval of the regression.

$$\Pr(d) = \frac{(\lambda_d)^d}{d} e^{-\lambda_d} \tag{2.9}$$

$$P(D) = 1 - P(ND) = 1 - \Pr(d = 0) = 1 - e^{-\lambda_d} \tag{2.10}$$

$$P(F) = 1 - e^{-M \cdot S \cdot \ln\left(\frac{F}{T_{defect}}\right)} \tag{2.11}$$

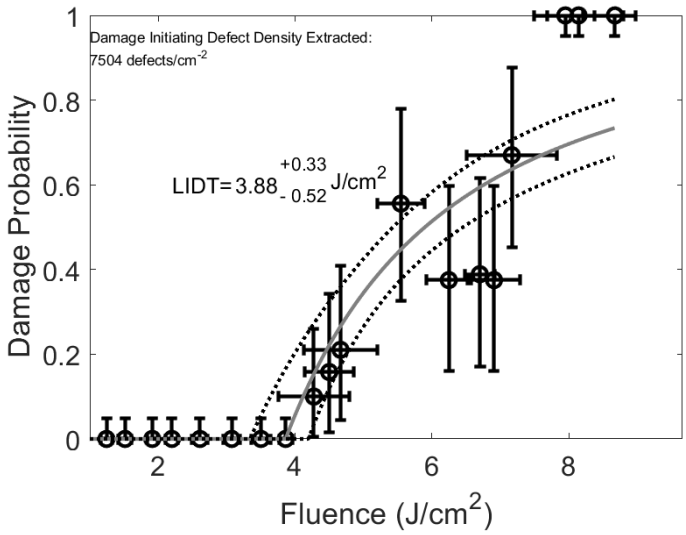

Figure 2.5) Example of measured LIDT data on an HfSiOx mixture, fit to the degenerate defect ensemble model developed by Ref [98] equation 2.11.

The horizontal error bars are the standard deviation among 20 fluences measured on that test row. The vertical error bars are determined by integrating the 95% of the binomial probability density function, equation 2.12, at the measured probability p, for each fluence data point [95]. In equation 2.12, p is the measured damage probability at a fluence, k is the number of damaged test sites out of n number of test sites. The n/p term is the binomial coefficient. In words, integrating 95% of the area of equation 2.12 asks the question: "given a measured damage probability, p, from a test utilizing n number of test sites, what is the 95% confidence interval of probabilities that might be observed if an identical test was repeated". The asymmetry of the vertical error bars near 100% and 0% probability reflects the intuition that it is impossible to have a probability greater than 1 or less than 0.

$$PDF_P(k|(n,p)|) = \binom{n}{p} p^k (1-p)^{n-k} \tag{2.12}$$

Next, the practical aspects of a LIDT test setup will be introduced. The ISO-21254

international standard for laser damage testing provides a set of guidelines that all laser damage tests should conform to [18]. Specifically, the ISO standard outlines the necessary components of an LIDT test bench, as well as setting limits on acceptable beam profile, beam size, beam size stability, and energy stability. Also, the standard provides a set of equations used to calculate temporal profile, spatial profile, and gaussian beam effective area corrections necessary to report an accurate damage threshold. The expression for effective gaussian beam area A_{eff}, is shown in equation 2.6. The effective area is the ratio of the total pulse energy, E, to the maximum energy density, H_{max}. This ratio is calculated by integrating the beam profile and dividing it by H_{max}. In equation 2.6, $d_{1/e2}$ is the beam diameter at $1/e^2$ of maximum intensity, F_{max} is the maximum energy density in the profile. The fluence for that shot is the total pulse energy, E, divided by the effective area, A_{eff}. The significance of equation 2.6 is there is a factor of ½ between the $1/e^2$ area and the effective area.

$$A_{eff} = \frac{E}{H_{max}} = \frac{\left(H_{max} \int_{-\infty}^{\infty} \int_{-\infty}^{\infty} e^{-\frac{8(x^2+y^2)}{d_{\frac{1}{e^2}}}} dxdy \right)}{H_{max}} = \frac{1}{8}\pi d_{\frac{1}{e^2}}^2 \qquad (2.6)$$

The key requirements of the ISO standard are summarized in the following section [18]. More requirements exist, but these requirements guide the most important parts of designing a LIDT testing setup. First, the beam profile shall not be smaller than 200um unless the laser energy is not high enough to achieve damaging fluences. The beam profile shall be analyzed at several positions close to the focus to assure the sample is in the center of the waist. The energy and polarization should be controlled with an appropriate rotatable waveplate system, typically combined with thin film polarizing mirrors. Damage detection should be performed by inspecting the optic

surface with a Nomarski type differential interference contrast microscope with a magnification of at least 10x. Damage is defined as any observable change in the surface after laser irradiation. For tests involving more than one shot per site, an online (i.e *in situ)* damage detection must be used. Suitable online damage detection techniques include: co-incident CW laser beam coupled with a scatter detection camera or photodiode, online microscope techniques, photoacoustic detection, and/or photothermal detection.

The LIDT testing setup implemented for this work is shown in figure 2.6. Laser damage measurements were performed using a Q-switched Nd:YAG laser (Quanta Ray) with third harmonic generation, producing pulses of 355nm wavelength. The pulse width was measured by fast rise time photodiode and was 8ns FWHM. The repetition rate of the laser is 10Hz. The polarization state was linear, s polarized. A gaussian beam is focused using a 1m focal length lens to a size of ~220μm at $1/e^2$. Energy detection and beam profile are measured on each shot from beamsplitters BS1 and BS2. Energy is controlled by the motorized half wave plate in combination with the thin film polarizers. Automated damage procedure is controlled by the PC. The low fluence tests are performed first to prevent ejected material from affecting future test sites. To move the optic to a new test site, the XY motorized stage is translated laterally.

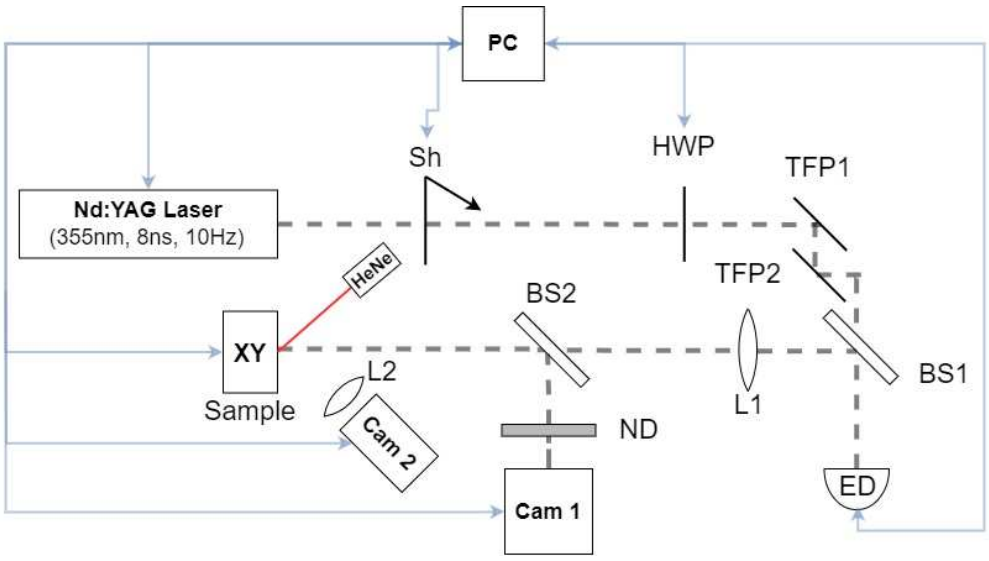

Figure 2.6 Sh: fast motorized shutter, HWP: half wave plate, TFP1/2: thin film polarizers, BS1/2: beam splitter, L1: 1m focusing lens, L2, Scatter light lens, Cam1: beam profile camera, Cam2: scatter detection camera, HeNe: Helium-Neon CW damage detection laser, XY: motorized sample stage, ED: energy detector, ND: neutral density filter

The damage tests performed on amorphous oxide thin films using the setup above used the 1-on-1 protocol because the pointing stability of the Nd:YAG laser was too large to implement S-on-1 tests. When the beam position has shot to shot variation, an effect known as pseudo-statistical accumulation occurs which decreases the S-on-1 damage threshold but is not reflective of the true material properties [5]. Therefore, a set of samples fabricated by BTD, IBS, and EBE were sent to Lidaris for multi-pulse 355nm LIDT measurements. These samples include: 2-layer AR's containing $Hf_{0.63}Si_{0.37}O_x$, and $Hf_{0.64}Al_{0.36}O_x$, IBS HfO_2/SiO_2 HR, an EBE AR, and an EBE HR. Lidaris measured the LIDT in a 1-on-1, 10-on-1, 100-on-1, 1000-on-1, and 10000-1 scheme. In these tests the beam size was 220-230μm, pulse width was ~5+/- 0.5ns, and repetition rate was 100Hz. The difference in pulse width between the testing setups was 3ns, which gives the expectation that the LIDT measured at Lidaris should be lower than the LIDT measured internally. This is informed by the TE model pulse width dependence, equation 1.11.

2.3.2 Laser Conditioning

Laser conditioning consists of irradiating a test optic at a fluence below the damage threshold, but high enough to cause a material change that improves the laser damage resistance upon further irradiation. In pulsed laser systems this can be implemented by performing the R-on-1 LIDT test, where the fluence is ramped from low to high on a single test site [7]. In this thesis, laser conditioning is executed by performing a raster scan of the entire optic with 90% fluence overlap between laser pulses. The raster scan laser conditioning has been shown to improve the LIDT by a factor of 2-4 [45,51,4,55]. The conditioning fluence is chosen to be close to 50% of the measured LIDT of that coating. Raster scan conditioning was performed on a single layer of HfO_2 fabricated by BTD and IBS, a UVFS substrate, and a $Hf_{0.56}Si_{0.44}O_x/SiO_2$ AR coating fabricated by BTD.

The literature has established that laser conditioning increases the laser damage threshold of a given optic, but the reported mechanism of the improvement varies from study to study [35,45-55]. References [35,98], report the following mechanism, depicted in figure 2.7 where a_0 and F_0 are the defect radius and threshold fluence of the "weakest" defect, which is at the minimum point of the curves. If laser irradiation at a fluence below F_0, F_c, heats the absorber and surrounding area to a temperature exceeding the melting point of both the defect and the host, the defect will disperse into the host medium, and laser conditioning occurs. This effectively removes any defects with a radii between a^c_{min} and a^c_{max}. This mechanism of laser conditioning aligns with the empirical result that dense IBS films do not improve with laser conditioning, while porous EBE films consistently improve with laser conditioning. The reason being that the melted defect cannot diffuse into the dense host material [35]. Alternatively, in the case of thick HR coatings, *Papandrew et al* demonstrated that laser conditioning ejects nodular

defects, and the ejected area has a lower photothermal absorption signal after nodule ejection [55]. Technically, nodule ejection is a laser damage event as classified by ISO 21254, but is not a functional damage event [18,72].

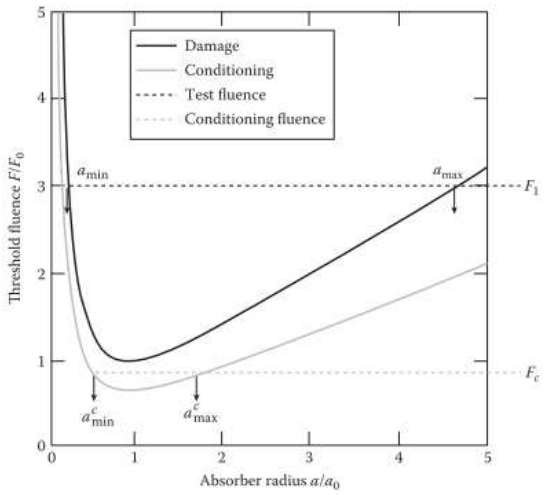

Figure 2.7 Damage thresholds and conditioning threshold curves vs. absorbing defect radii.

There are papers in the literature that suggest laser conditioning causes sub-stoichiometric metal compounds to bond with oxygen, which may change the defect ensemble [54]. The most commonly discussed mechanism, with little experimental evidence, is the evacuation of forbidden gap defect states to the conduction band, followed by a permanent relaxation to the valence band [7].

Chapter 3 Laser damage of UV hafnia-based multilayer dielectric coatings at 355 nm wavelength

Mega-Joule ultraviolet nanosecond pulses were used to demonstrate ignition at the National Ignition Facility in Dec. 2022 [106]. Scaling in energy relies, in part, on significant improvements in the UV multi-layer dielectric (MLD) coatings which damage more frequently due to UV backscatter from the target. This paper reports on the laser damage behavior of MLD coatings based on HfO_2, SiO_2, and Al_2O_3 designed for operation at λ=355 nm. Two-layer anti-reflection (AR) coatings were designed and fabricated by reactive biased target deposition (BTD) using mixtures of HfO_2 and SiO_2, HfO_2 and Al_2O_3, as the high index layer. The laser damage response was assessed from 1-on-1 and S-on-1 tests from which the laser induced damage threshold (LIDT) fluence was determined. It is shown that in BTD ARs which contain mixtures, $Hf_{1-y}Si_yO_x$ and $Hf_{1-y}Al_yO_x$ in the high index layer, the 1-on-1 LIDT increases with respect to HfO_2/SiO_2 AR. The BTD ARs have a density higher than electron beam evaporated (EBE) HfO_2/SiO_2 ARs but lower than ion beam sputtered (IBS) HfO2/SiO2 ARs. It is shown that the 1-on-1 LIDT of the BTD ARs is slightly lower than that of electron beam evaporated (EBE) HfO_2/SiO_2 ARs and ion beam sputtered (IBS) HfO_2/SiO_2 ARs. While the 10^4-on-1 LIDT of EBE ARs was higher than that of either sputtering method. Substrate etching prior to deposition and UV conditioning increase the 1-on-1 LIDT of sputtered ARs. The S-on-1 LIDT of BTD ARs decreases by ~25% for S=10 and remains unchanged to S=10^4 laser shots, indicating no accumulation fatigue.

---

[1]Significant portions of this chapter have been reproduced with permission from Maxwell Weiss, A. Davenport, S. C. Lucs, D. Pamedytytė, J. Galinis, A. Melninkaitis, J. Siehien, W. Siehien, M. Chicoine, F. Schiettakatte, C. S. Menoni, manuscript to be submitted to Applied Optics

3.1 Introduction

Two megajoules of λ=350 nm UV laser light with a peak power of 500 TW focused on the fusion target were necessary to create the x-rays that indirectly drove the capsule implosion, and which resulted in ignition [106]. In this landmark experiment at the Lawrence Livermore National Ignition Facility (NIF) an energy gain of 1.5 was obtained. Subsequent experiments that followed have demonstrated higher gains have accelerated research to advance critical technologies which will pave the way for inertial fusion to become a practical source of carbon-free energy [134].

One of these critical technologies are the interference coatings in the laser architecture which damage prematurely. In the NIF laser there are about 800 optics that route 192 laser beams of λ=1053 nm (1ω) and a few nanoseconds duration into the final optics assemblies which condition the beams, frequency up-convert them to 3ω, and focus them into the target. Many of these optics are coated with dichroic dielectric coatings which are prone to UV laser damage. As an example, UV damage due to backscattered λ=351 nm laser light is the dominant cause of damage on the last 1ω turning mirrors that guide the beams into the final optics assemblies [6]. This illustrates the challenges to achieving superior laser damage resistance in the UV. The demands on the coatings projected for laser drivers in a fusion power plant to survive 10's of gigashots adds additional challenges to the engineering and testing of the dielectric coatings in critical components of kJ class lasers.

UV dielectric coatings for lasers producing nanosecond pulse duration, such as NIF and OMEGA, are typically designed using HfO2 and SiO2 thin films as low and high refractive index material respectively. There are experiments that show replacing HfO2 by HfAlOx and HfSiOx mixtures improves laser damage performance [2,5,8,126].

Amorphous oxide mixtures provide flexibility for tailoring the optical bandgap and the refractive index while affecting atomic bonding and hence the structural properties of the thin films [17,105,119,135]. The reasoning behind selecting larger optical bandgap materials for the high index layer in multilayer dielectric coatings (MLD) containing SiO2 as the low index layer is that within the framework of the model of laser damage, the multiphoton absorption and avalanche ionization rate decreases [35]. However, the benefits associated with this strategy are counter-balanced by the needs to increase the number of layers in the stack to meet the same spectral requirements [6]. Depending on the deposition process, thicker coatings are more prone to nodule incorporation which can cause electric field intensification and subsequently degrade laser damage performance [52]. UV damage is also affected by the presence of intrinsic defects, i.e. oxygen traps, which density and type of defects vary with deposition process [1].

Several publications have reported conflicting trends in the threshold fluence, the laser induced damage threshold (LIDT), at which UV coatings damage when the pulse duration is of the order of nanoseconds. Studies on single layers have reported the nanosecond LIDT weakly correlates with band gap for Hf1-ySiyOx mixtures [2,5,127]. Meanwhile, stronger correlations were found in high reflection (HR) coatings [39,88,40]. As discussed in [100], the nanosecond LIDT trends with oxide mixture concentration appear to be more complex than in the base materials, where a rate equation model does not predict laser damage behavior and additional mechanisms need to be considered. Beyond intrinsic material processes, there are other mechanisms that influence the LIDT of UV coatings. In particular in MLD stacks containing only a few layers the influence of imperfections at the substrate reduces the LIDT. Ref [123] demonstrated that residual contamination from polishing with CeO2, and subsurface defects (SSD) can decrease the LIDT of AR coatings by a factor of 3.4, which may explain

the conflicting results between HRs and ARs due to the difference in field strength at the substrate interface.

In this paper we describe results of laser damage studies on UV coatings designed for λ=355 nm. As discussed in section 1.1.3, the mirror coatings used in NIF have multiple wavelength requirements, namely anti-reflection at 3ω and high reflection at 1ω. Investigating the 3ω laser damage behaviors of coatings designed for 3ω provides the similar information as investigating the 3ω laser damage to 1ω/3ω dichroic mirrors, the only difference would be the standing wave electric field distribution in the coating which could be higher or lower throughout the coating depending on the design. Moreover, the NIF mirrors do not experience simultaneously illumination from 1ω and 3ω light. The experiments were motivated by the need to identify differences in the laser damage behavior when the composition of the high refractive index layer in AR stacks is varied, and to understand the impact of laser conditioning and substrate modifications prior to deposition on the laser damage behavior. We also compare the laser damage behavior of ARs of HfO2/SiO2 of identical coating designs deposited by different processes. Two-layer AR coatings containing mixtures of Hf1-ySiyOx and Hf1-yAlyOx as the high index layer and SiO2 as the low index layer were reactively sputtered by biased target deposition (BTD). X-ray photoelectron spectroscopy (XPS), scanning transmission electron microscopy with electron energy loss spectroscopy (STEM-EELS), Rutherford backscattering (RBS), and glancing angle x-ray diffraction (GI-XRD) were utilized to better understand the properties of mixture alloys. Assessment of the ARs 1-on-1 laser damage behavior shows there is a significant improvement in the LIDT when the content of Si in the HfO2 mixture is large, ~ 80%. For mixtures with a Si or Al content below 50%, the AR LIDT is upmost 20% higher than that of the HfO2/SiO2 AR. Substrate etching improved ARs LIDT while UV laser conditioning was less effective. The

BTD ARs showed a fatigue behavior in which the S-on-1 LIDT decreased by ~25% for S=10 and then remained constant to S=10^4. The deposition process influences the 3ω ARs LIDT as has been found previously [41] with IBS coatings showing the highest 1-on-1 LIDT. For comparison we also describe the damage behavior of HR HfO2/SiO2 coatings deposited by ion beam sputtering (IBS) and electron beam evaporation (EBE).

3.2 Experimental methods

3.2.1 Fabrication and characterization

The following anti-reflection coatings were fabricated by reactive BTD deposition which allows co-sputtering of several targets using the 4Wave.Inc Laboratory Alloy Nanolayer System (LANS). The deposition parameters are shown in Table 1. Atomic ratio subscripts shown are taken from RBS measurements. $Hf_{1-y}Si_yO_x$ mixtures were fabricated with high, medium, and low concentrations of SiO_2. A single $Hf_{1-y}Al_yO_x$ mixture was tested with a moderate Al concentration. The high SiO_2 concentration mixture was tailored to have the same refractive index as Al_2O_3 for direct comparison of laser damage resistance with a constant index.

Table 3.1: Deposition parameters for high index materials used in AR coatings

Material	Deposition Rate (nm/s)	Target Voltage (V)	Target Current (mA)	Hf Target Duty Cycle	Second Target Duty Cycle	Pulse Frequency (kHz)	O_2 flow (sccm)
$Hf_{0.64}Al_{0.36}O_x$	0.0137	-800	192	98%	75%	10	7
$Hf_{0.2}Si_{0.8}O_x$	0.0250	-900	157	50%	85%	50	10
$Hf_{0.56}Si_{0.44}O_x$	0.0187	-900	193	75%	60%	50	10
$Hf_{0.63}Si_{0.37}O_x$	0.0197	-800	145	98%	60%	10	7
$Hf_{0.73}Si_{0.27}O_x$	0.0195	-900	191	90%	60%	50	10
HfO_2	0.0111	-900	119	90%	N/A	50	10
SiO_2	0.0174	-800	47	N/A	90%	10	5
Al_2O_3	0.0075	-900	108	N/A	80%	50	10

The base pressure of the deposition system was 10^{-8} Torr while the operating chamber pressure was 10^{-4} Torr (Argon and Oxygen). All materials were sputtered from metallic targets of hafnium, silicon, and aluminum. The target geometry as described in [99] consists of a 6-sided target fixture, with the substrate stage at the center. The target voltage +10V/-900V was pulsed at a high frequency to prevent target arc events. The mixture concentration was controlled by selecting the duty cycle of each metal target individually on a 3-channel pulsed voltage source. The ARs, deposited onto UV fused silica substrates, were designed for an angle of incidence (AOI) of 0 degrees. SiO_2 was used as the low index layer in all AR coatings. The standing wave electric field distribution was simulated using OptiRe™. The peak optical intensity inside the high index layer occurs at the substrate interface and in all coatings this value is ~66% of the incident intensity (Supplementary Material Fig S1).

Reference AR coatings were also produced by IBS and EBE. The parameters of the IBS deposition were: accelerator grid voltage of 1250V, beam current of 600mA, and oxygen flow of 13 sccm directed at the target. HfO_2 was sputtered from a metallic hafnium target, while the SiO_2 was sputtered from an oxide target. The pressure in the system prior to starting the ion sources was ~10^{-7} Torr, and ~10^{-4} Torr during deposition. The deposition rate of hafnia/silica was ~0.16/~0.22 nm/s respectively. The EBE process used an end-Hall plasma assist source at 100V and 2A ion current during deposition. The base pressure was 9×10^{-6} Torr, and an oxygen backfill pressure of 10^{-4} Torr was applied during deposition to improve stoichiometry. Using the same conditions in the IBS system a quarter wave 40-layer HfO_2/SiO_2 HR with 99.99%. reflectivity at λ=355 nm was fabricated. An EBE HR with a quarter-wave 34-layer design was also fabricated. Both the IBS and EBE HRs contain a 2λ SiO_2 capping layer.

To investigate the influence of substrate defects on the $Hf_{0.56}Si_{0.44}O_x/SiO_2$ AR and IBS HfO_2/SiO_2 AR damage behavior, the substrates were etched ~200 nm in vacuum using an Ar/O mixed plasma at 200V prior to coating deposition, in accordance with the optimal result of [123].

The optical properties of the samples were determined from spectroscopic ellipsometry and spectrophotometry. Details of these measurements are provided in the supplementary material. Using the Lorenz-Lorenz effective medium approximation, the degree of porosity of the AR layers was determined.

The composition of the high and low index layers of the ARs deposited by BTD, IBS and EBE, the layer density, and the Ar content in the thin films were determined by Rutherford Backscattering (RBS) using conditions described in the supplementary material. X-ray Photoelectron Spectroscopy (XPS) was used to identify the degree of mixing in the alloys. Scanning transmission electron microscopy with electron energy loss spectroscopy (STEM-EELS) measurements were performed on selected AR coatings by Eurofins Materials Science to gain insight on the nanomorphology of the mixture in the high index layer and at its interfaces with the low index layer. The degree of crystallization was investigated by Glancing Incidence X-Ray Diffraction (GI-XRD). Details of these measurements are provided in the Supplementary Material.

3.2.2 Laser Induced Damage Threshold Testing

1-on-1 laser damage tests were performed using an Q-switched Nd:YAG laser with third harmonic, λ=355 nm, generated by upconversion in two KDP crystals. The pulse width was measured by a fast rise time photodiode to be 8 ns FWHM. The repetition rate of the laser is 10Hz. The 1-on-1 damage protocol described by ISO 21254-1 was utilized with offline damage detection by Nomarski microscope with 40x magnification

[18]. The polarization state was linear, s polarized, but the angle of incidence was 0 degreees. The laser beam was focused using a 1m focal length lens to a $1/e^2$ beam diameter of ~220μm. Energy detection and beam profile are measured on each shot. Energy is controlled by a motorized half wave plate in combination with thin film polarizers. Automated damage procedure is controlled by the PC using MATLAB. Damage threshold determination is performed using the degenerate defect ensemble model [95].

A set of samples fabricated by BTD, IBS, and EBE were sent to Lidaris for multi-pulse S-on-1 LIDT tests. These samples include, 2-layer AR's containing $Hf_{0.63}Si_{0.37}O_x$, and $Hf_{0.64}Al_{0.36}O_x$, IBS HfO_2/SiO_2 HR, an EBE AR, and an EBE HR. Lidaris measured the LIDT in a 1-on-1, 10-on-1, 100-on-1, 1000-on-1, and 10000-1 scheme. In these tests the $1/e^2$ beam diameter was 200-230μm, pulse width was ~5+/- 0.5ns, and repetition rate was 100Hz.

Raster scan laser conditioning was performed using a 90% fluence overlap across the entire coating after deposition. The raster scan fluence was chosen to be below the measured LIDT of that specific coating and close to half this value. Before and after conditioning the optic was inspected with a Nomarski microscope at 20× magnification and no significant damage sites were found. The transmission spectrum was measured after treatment, but no change was observed. After raster conditioning, the coating was LIDT tested using the 1-on-1 damage measurement described above.

3.3 Results and discussion

The optical constants of the materials in Table 1 are shown in Fig. 1a. As the SiO_2/Al_2O_3 content into HfO_2 increased, the index of refraction decreased following the Lorentz-Lorenz mixing rules [19]. The transmission vs photon energy of the single layer

materials is shown in Fig. 1(b). Using the 80% transmission cut-off as a measure of the optical bandgap, Fig. 1(b) shows all materials are transparent at a photon energy of 3.5 eV (λ=355 nm).

The porosity, obtained from the data of Fig. 1a, as described in the Supplementary Material, is highest in EBE SiO_2 and lowest in IBS SiO_2 as illustrated in Fig. 1c. The atomic density of Si atoms determined by RBS in the single layer SiO_2 films is inversely related to the porosity. The RBS results indicate an argon concentration of 2-5% in the BTD films and of ~3% in IBS single layers, similar to values reported for other IBS films [97]. See Fig. S2.

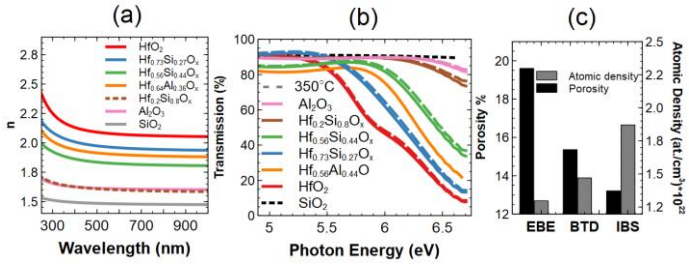

Fig. 3.1. (a) Dispersion of the refractive index of the high index materials from Table 1; (b) Transmission at the band edge versus high index material; (c) Porosity and atomic density of SiO_2 fabricated by EBE, BTD, and IBS.

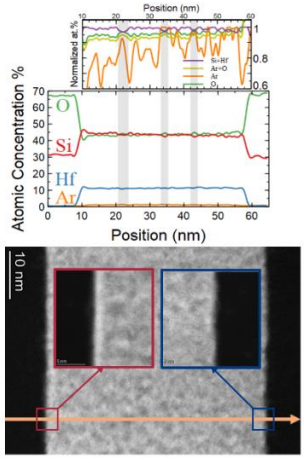

Fig. 3.2. HAADF TEM-EELS image and line scan of the $Hf_{0.56}Si_{0.44}O_x/SiO_2$ AR fabricated by BTD. Middle plot shows atomic concentrations of O, Si, Hf, and Ar throughout the AR stack. The Upper plot is the atomic concentration of (Hf+Si), Ar,O and (Ar+O) normalized to their maximum value in the line scan. Grey zones indicate nanoscale voids where (Ar+O) concentration is at a peak and (Hf+Si) is at a local minimum.

The results of STEM-EELS measurements performed on $Hf_{0.56}Si_{0.44}O_x$ are shown in Fig. 2. The bright field images illustrate the nanoscale morphology commonly observed in sputtered films [97,132,9]. The dark regions indicate nano-voids. The line scan profile shows that the normalized atomic percentage of Hf+Si decreases in the positions where Ar+O% is at a local peak, indicated by the grey bars. The presence of an oxygen gas in the voids is concluded from RBS measurements where this particular material had an oxygen to metal ratio (O: Hf+Si) of 2.2. This behavior is common among amorphous oxides deposited by BTD as shown in TiO_2:Ta_2O_5 mixtures [105].

All BTD mixture materials were amorphous as deposited, as shown in Fig. S4. The only exception was BTD HfO_2 which showed signs of crystallization. The $Hf_{1-y}Si_yO_x$ and $Hf_{1-y}Al_yO_x$ alloys remained amorphous to 600˚C. Literature has demonstrated $Hf_{1-y}Si_yO_x$ mixtures with SiO_2 content greater than 20% do not show signs of crystallization at temperatures ≥900˚C [40].

The 1-on-1 LIDT of AR coatings fabricated by BTD vs the transmission cutoff is shown in Fig. 3. The lowest 1-on-1 LIDT is that of the HfO_2/SiO_2 AR, with a value of 2.8 J/cm2, in good agreement with Gallais *et* al [41]. The highest LIDT is that of the Al_2O_3/SiO_2 AR. Using these two data points, a linear scaling of the 1-on-1 LIDT with the transmission cutoff is shown by the solid line in Fig. 3. Using this as reference, the LIDT of the mixture ARs with Si or Al content of ~ 50% shows a lower increase in LIDT than predicted. Instead, in mixtures with a Si content is 0.27 and 0.8, the 1-on-1 LIDT follows the predicted increase with band edge. In all cases, annealing at 350˚C improves the LIDT, albeit a small improvement.

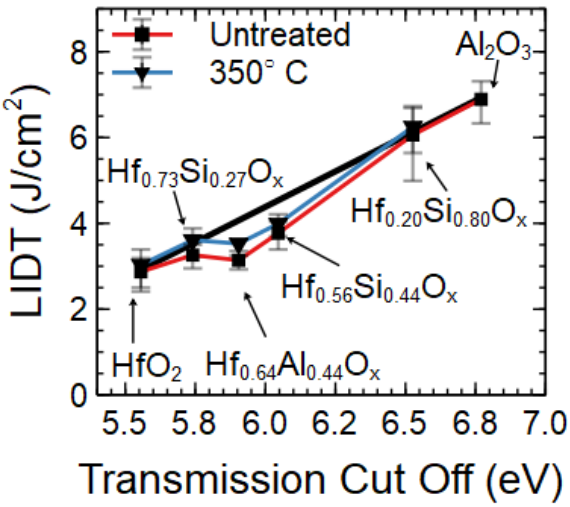

Fig. 3.3 (a) 1-on-1 LIDT vs transmission cut-off of AR coatings. The 80% transmission cut off defined as the UV photon energy where transmission drops to 80% using data from Fig 2b is taken as a measure of the optical bandgap. The solid line is the expected scaling of the 1-on-1 LIDT with band edge obtained using the values of the LIDT of the HfO_2/SiO_2 and Al_2O_3/SiO_2 ARs.

The results of Fig. 3 suggest that, in spite of the fact that the alloys seem to be homogeneously mixed and contain a significant proportion of Hf-Si(Al)-O bonds as shown by XPS and EELS, there are other factors that reduce the 1-on-1 LIDT when the proportion of the two cations in the oxide is about the same. One possibility is that there is a higher density of defects, i.e. metallic and suboxide particles, that reduce the LIDT. The XPS analysis of the $Hf_{1-y}Si_yO_x$ mixture however could not resolve suboxide features. See Fig. S3 in Supplementary Material. Previously studies reported a similar behavior in mixture single layers [100,41]. The damage mechanism of the ARs in the 1-on-1 tests is defect initiated [73], as can be inferred from the presence of numerous, unconnected microscale pits [2]. See Fig. S7 in Supplementary Material. All BTD AR coatings exhibited this damage morphology.

Figure 3.4 (a) shows the S-on-1 LIDT of the BTD $Hf_{0.63}Si_{0.37}O_x$ and $Hf_{0.64}Al_{0.38}O_x$ AR coatings and it compares their behavior to that of EBE and IBS HfO_2/SiO_2 ARs. As the figure shows the 1-on-1 LIDT is ~21% lower than both the HfO_2/SiO_2 EBE AR, 4 J/cm^2, and the IBS HfO_2/SiO_2 AR, 3.9 J/cm^2.

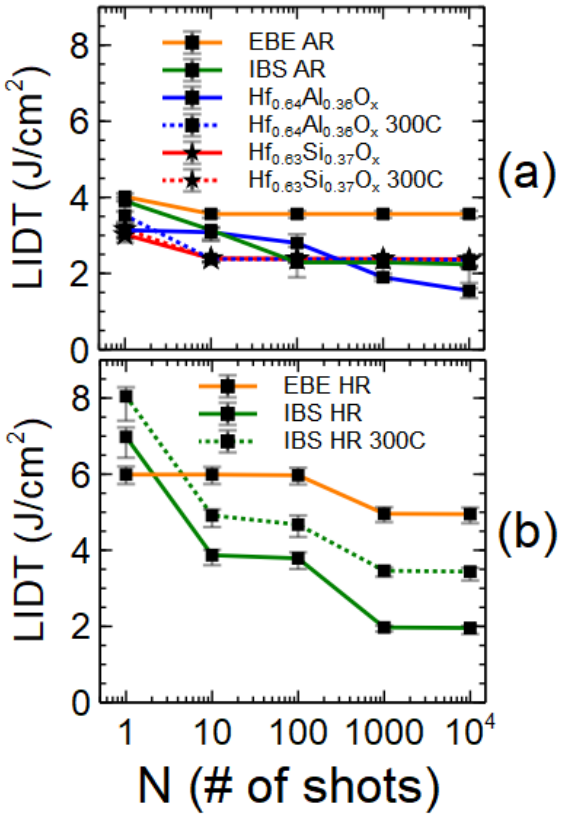

Fig. 3.4.) S-on-1 LIDT versus S number of pulses from 1 to 10^4 shots. (a) AR coatings (b) HR coatings.

The S-on-1 LIDT of the BTD $Hf_{0.63}Si_{0.37}O_x$ and $Hf_{0.64}Al_{0.36}O_x$ ARs is peculiar, as it drops from ~3 J/cm² to ~2.3 J/cm² for S=10 and then it remains constant to S=10^4. Annealing to 300 °C does not significantly alter the LIDT, except in $Hf_{0.64}Al_{0.36}O_x$. For comparison, Fig. 3.4b shows the S-on-1 LIDT behavior of the IBS and EBE HfO_2/SiO_2 HR coatings. In the IBS HR the LIDT decreases ~2-3x from S=1 to S-10^4. Instead, the change in the EBE HR is 17%. Interesti.ngly, annealing the IBS coating increased in LIDT for all S-on-1 tests, but did not change the multi-pulse LIDT trend. The mechanism of fatigue effects in multi-pulse laser damage could be of different origin, i.e. changes in the electronic/chemical structure of defects [26], pulse to pulse thermal accumulation [27], laser induced defect generation [35], long-lasting (~100ms) defect state lifetimes [1,44], and pseudo-statistical fatigue [28,29]. Discerning the relative contribution of the

fatigue mechanisms in our samples is not possible, but the change in fatigue behavior of the IBS coating with annealing indicates a fatigue resulting from sub-stoichiometric bonds.

Comparing the 10^4-on-1 LIDT of coatings by different fabrication methods we find that the denser sputtered IBS coatings demonstrate lower multi-shot laser damage resistance compared to the more porous EBE coatings. This could be due to process variation, but literature suggests a fundamental property of the fabrication process may causing the lower damage threshold of the IBS sputtered films [79,89]. Previous work has suggested the incorporation of Ar in the IBS coatings could lead to reduced LIDT [97,132]. EBE films have columnar pores which do not encapsulate process gasses [9].

The 3ω LIDT of AR's deposited on etched and non-etched substrates are depicted in Fig. 4a. The 3.7× increase in LIDT of the bare substrate proves the substrate polishing residuals are the fluence limiting defect of the substrate. In the $Hf_{0.56}Si_{0.48}O_x$ AR coating deposited by BTD a small increase of 1.1 times was observed, while the IBS AR increased by nearly 2 times. This indicates the substrate polishing residuals are not the fluence limiting defect of the BTD mixture AR. The etched substrate testing on the IBS AR agrees with *Abromavičius et al* where the 3ω LIDT of AR coatings deposited on plasma etched substrates was larger, but our reported factor of ~2x is less than the 3.4 times improvement reported [123]. Regardless, this experiment demonstrates that the fluence limiting defect of AR's may be polishing residuals, as has also been shown in ARs deposited in Yb:YAG crystals [136]. Considering that at the substrate/coating interface the electric field strength is the highest, it is unsurprising that removing the substrate defects has a large impact on LIDT. Substrate defects in the form of remnants of CeO_2 from the polishing slurry with a ~3eV band gap of CeO_2, can efficiently absorb the 3ω=3.49eV photons in a single photon process and reduce LIDT.

Table 3.2. Samples used for laser conditioning tests, the associated 1-on-1 LIDT of that sample, the conditioning fluence, and the change in 1-on-1 LIDT post conditioning.

Sample	1-on-1 LIDT (J/cm^2)	Raster Scan Fluence (J/cm^2)	1-on-1 LIDT change post conditioning
BTD HfO_2	2.78	1.5	+54% +/- 4.9/6.7
BTD $Hf_{0.56}Si_{0.44}O_x$	3.43	1.7	+31% +/- 9.5/12.2
IBS HfO_2	5.38	3.0	+11% +/- 2.9/4.9
UVFS	22.2	14	-2% +/- 3.5/5.3

In Table 3.2 the ratio of conditioned to unconditioned LIDT for the BTD HfO_2 and $Hf_{0.56}Si_{0.44}O_x$ samples was calculated to illustrate a change in damage threshold due to conditioning. The error bars of the pre-post LIDT on IBS HfO_2 overlap indicating almost no change in damage threshold. The laser conditioning tests demonstrate this technique is ineffective in the IBS films, in agreement with [45]. The UVFS substrate damage threshold did not change significantly following laser conditioning which is evidence that laser conditioning is affecting the film rather than the substrate interface. The 54% increase in BTD HfO_2 is a significant improvement, but results from the literature indicate e-beam coatings can improve by a factor of ~2-3x [45,51,54,55]. Combining this observation with the lack of change in IBS films, the impact of laser conditioning may be inversely related to the density of the material. This aligns with the defect melting mechanism discussed in [35], where the defect cannot spread into the host effectively if the host material is dense.

3.4 Conclusion

The results of this work identified the role of composition of the high index layer in AR coating for λ-355nm and of deposition conditions in their laser damage response.

When the high index layer in the AR is a mixture, the LIDT improves over that of HfO_2. When the content of the two metal cations is similar, the LIDT is lower than the linear scaling of the LIDT with band-edge between HfO_2 and Al_2O_3. This is not surprising because in amorphous oxide mixtures with similar cation content, competition for oxygen can result in an alloy which contains metallic nanoclusters of either cation, and and/or many oxygen defects which in both cases would reduce the LIDT. Within the spatial resolution of STEM-EELS metallic nanoclusters were not observed. The contribution of non-lattice oxygen, which is observed in HfO_2, can not be separated in the XPS spectra of the mixtures. However, EELS data suggests oxygen/argon interstitials are present in the voids of the $Hf_{0.56}Si_{0.44}O_x$ mixture, which in the context of [97,132], could explain the lower LIDT of this coating.

The BTD ARs have a similar value of the 1-on-1 LIDT as the EBE HfO_2 AR. Both materials are more porous than the IBS HfO_2 AR which showed the highest 1-on-1 LIDT. As well, the 10^4-on-1 LIDT of the EBE HfO_2 AR, was the highest. The S-on-1 laser damage behavior for the BTD and EBE ARs is also very similar. It decreases by about ~25% after S=10 shots and remains constant to S=10^4 shots. This behavior contrasts with that IBS HRs in which there a systematic decrease in the LIDT with pulse number. We speculated substrate defects dominated the S-on-1 LIDT of the sputtered ARs, and thus implemented substrate etching and UV conditioning, which favorably impacted the 1-on-1 LIDT.

Chapter 4

Summary and Outlook

We present the first report on the laser damage behaviors of amorphous oxide thin film AR coatings fabricated by biased target deposition. We demonstrated an improved LIDT in BTD ARs fabricated using mixture coatings in the high index layer over BTD HfO_2 ARs. Increasing silica or alumina concentration in hafnia decreased the refractive index but increased the band gap, although not at the rate of increase predicted from the bandgap values of HfO_2 and Al_2O_5. Dopant addition above 10% also suppressed crystallization of BTD HfO_2. Mixtures also enabled higher temperature annealing without crystallization. Annealing blue shifted the UV transmission edge, and increased LIDT. Among 2-layer AR coatings, HfO_2 fabricated by BTD had the lowest 1-on-1 LIDT (2.78 J/cm^2). Meanwhile, the Al_2O_3 AR coating had the highest 1-on-1 LIDT. A comparative analysis of fabrication methods was performed between BTD, IBS, and EBE. Using the refractive index, it was determined that the porosity of EBE films is the greatest, while IBS was the least porous. The BTD films had a porosity in between IBS and EBE. Comparison of LIDT data among fabrication methods indicates that EBE coatings have the best multi-shot laser damage, while IBS coatings have higher 1-on-1 LIDT. In fusion energy applications higher multi-pulse LIDT is beneficial, hence the use of porous deposition technologies (EBE or sol-gel) in large aperture MLD coatings [6]. BTD AR coatings performed slightly lower than IBS or EBE in all categories. A mechanism for the reduced performance of BTD coatings compared to IBS requires further research. Considering the current NIF operating fluence of 8 J/cm^2 [68] improvements in the AR coatings demonstrated in this work is needed. A raster scan

conditioning protocol demonstrated improved LIDT in both BTD and IBS films. The improvement by laser conditioning was greater in BTD films. However, the laser conditioning improvements were small compared to the improvements typically demonstrated on EBE films or optical crystals [45,51,55]. From this result, we conclude that the effectiveness of laser conditioning may be inversely related to the density of the film.

The role of the substrate in the laser damage of AR coatings was illustrated, where AR coatings deposited on dry etched UVFS substrates demonstrated an improvement in LIDT. From this result, we conclude that the polishing residuals on the critical substrate interface contributes to the damage behaviors anti-reflection coatings and single layers. This has implications for the interpretation of any LIDT data where the high index material is in contact with a polished substrate. Furthermore, investigating higher band gap polishing slurries (such as Al_2O_3) may be a path to higher LIDT substrates in the UV wavelengths.

Bibliography

[1] S. Papernov *et al.*, “Optical properties of oxygen vacancies in HFO2 thin films studied by absorption and Luminescence Spectroscopy,” *Optics Express*, vol. 26, no. 13, pp. 17608–17623, Jun. 2018. doi:10.1364/oe.26.017608

[2] Q. Zhou *et al.*, “Role of nano-precursors in ultraviolet-laser damage of HFO2/SiO2 mixture coatings,” *Thin Solid Films*, vol. 739, p. 138963, Dec. 2021. doi:10.1016/j.tsf.2021.138963

[3] M. R. Kozlowski, “Large area laser conditioning of dielectiic thin film mirrors,” *Laser-Induced Damage in Optical Materials 1989*, Nov. 1990. doi:10.1117/12.2294446

[4] I. B. Angelov, M. von Pechmann, M. K. Trubetskov, F. Krausz, and V. Pervak, “Optical breakdown of multilayer thin-films induced by ultrashort pulses at mhz repetition rates,” *Optics Express*, vol. 21, no. 25, p. 31453, Dec. 2013. doi:10.1364/oe.21.031453

[5] F. R. Wagner, C. Gouldieff, J.-Y. Natoli, and M. Commandré, “Nanosecond multi-pulse laser-induced damage mechanisms in pure and mixed oxide thin films,” *Thin Solid Films*, vol. 592, pp. 225–231, Oct. 2015. doi:10.1016/j.tsf.2015.04.014

[6] C. J. Stolz, J. Weng, T. Teklemarim, M. Brophy, and P. Kupinski, “Evaluation of alumina and silica coating materials for the NIF final turning mirrors,” *Laser-Induced Damage in Optical Materials 2021*, Dec. 2021. doi:10.1117/12.2598577

[7] L. Ramalis, R. Buzelis, G. Dolmantaitė, and T. Tolenis, “Near fundamental nanosecond laser damage resistance of nanostructured all-silica mirrors at 355 nm by local laser irradiation,” *Results in Optics*, p. 100616, Jan. 2024. doi:10.1016/j.rio.2024.100616

[8] J. Shi et al., “Effect of annealing on the properties of HFO2-Al2O3 mixture coatings for picosecond laser applications,” Applied Surface Science, vol. 579, p. 152192, Mar. 2022. doi:10.1016/j.apsusc.2021.152192

[9] V. N. Peters *et al.*, “investigation of UV, NS-laser damage resistance of Hafnia films produced by electron beam evaporation and ion beam sputtering deposition methods,” *Journal of Applied Physics*, vol. 130, no. 4, Jul. 2021. doi:10.1063/5.0053219

[10] C. J. Stolz, L. M. Sheehan, S. M. Maricle, S. Schwartz, and J. Hue, “Laser conditioning methods of Hafnia-silica multilayer mirrors,” *SPIE Proceedings*, Apr. 1999. doi:10.1117/12.344419

[11] L. Jensen, M. Jupé, and D. Ristau, “UV damage mechanisms in oxide high reflectors,” *Laser-Induced Damage in Optical Materials: 2008*, Oct. 2008. doi:10.1117/12.804407

[12] W. Liu *et al.*, “Investigations on single and multiple pulse laser-induced damages in AL2O3/sio2 multilayer dielectric films at 355 nm,” *Optical Engineering*, vol. 57, no.

12, p. 1, Sep. 2018. doi:10.1117/1.oe.57.12.121905

[13] M. Steinecke *et al.*, "Quantizing nanolaminates as versatile materials for optical interference coatings," *Applied Optics*, vol. 59, no. 5, Feb. 2020. doi:10.1364/ao.379131

[14] T. Willemsen, M. Jupé, M. Gyamfi, S. Schlichting, and D. Ristau, "Enhancement of the damage resistance of ultra-fast optics by novel design approaches," *Optics Express*, vol. 25, no. 25, p. 31948, Dec. 2017. doi:10.1364/oe.25.031948

[15] T. Willemsen, P. Geerke, M. Jupé, L. Gallais, and D. Ristau, "Electronic quantization in dielectric nanolaminates," *SPIE Proceedings*, Dec. 2016. doi:10.1117/12.2244828

[16] N. M. Kamble, R. B. Tokas, S. Thakur, and N. K. Sahoo, "Compositional analysis of HFO2: SIO2 composite thin films and its correlation with refractive index," *AIP Conference Proceedings*, May 2012. doi:10.1063/1.4732453

[17] M. A. Fazio, G. Vajente, L. Yang, A. Ananyeva, and C. S. Menoni, "Comprehensive study of amorphous metal oxide and Ta 2 O 5 -based mixed oxide coatings for gravitational-wave detectors," *Phys. Rev. D*, vol. 105, no. 10, p. 102008, May 2022, doi: 10.1103/PhysRevD.105.102008.

[18] *Lasers and laser related equipment-Test Methods for laser-induced damage threshold,* ISO-21254-1, Internation Organization for Standardization.

[19] O. Stenzel, "Optical coatings," *Springer Series in Surface Sciences*, 2014. doi:10.1007/978-3-642-54063-9

[20] M. L. Grilli *et al.*, "AL2O3/SIO2 and HFO2/sio2 dichroic mirrors for UV solid-state lasers," *Thin Solid Films*, vol. 517, no. 5, pp. 1731–1735, Jan. 2009. doi:10.1016/j.tsf.2008.09.047

[21] M. Mazur, D. Kaczmarek, J. Domaradzki, D. Wojcieszak, and A. Poniedzialek, "Influence of material composition on structural and optical properties of HFO2-tio2 mixed oxide coatings," *Coatings*, vol. 6, no. 1, p. 13, Mar. 2016. doi:10.3390/coatings6010013

[22] M. Zacharias and P. Streitenberger, "Crystallization of amorphous superlattices in the limit of ultrathin films with oxide interfaces," *Physical Review B*, vol. 62, no. 12, pp. 8391–8396, Sep. 2000. doi:10.1103/physrevb.62.8391

[23] H. Wang *et al.*, "Study of reactions between HFO2 and si in thin films with precise identification of chemical states by XPS," *Applied Surface Science*, vol. 257, no. 8, pp. 3440–3445, Nov. 2011. doi:10.1016/j.apsusc.2010.11.042

[24] L. Zhao, S. Clima, B. Magyari-Köpe, M. Jurczak, and Y. Nishi, "*ab initio* modeling of oxygen-vacancy formation in doped-hfox RRAM: Effects of oxide phases, stoichiometry, and Dopant concentrations," *Applied Physics Letters*, vol. 107, no. 1, Jul. 2015. doi:10.1063/1.4926337

[25] N. Kaiser *et al.*, “Defect-stabilized substoichiometric polymorphs of hafnium oxide with semiconducting properties,” *ACS Applied Materials & Interfaces*, vol. 14, no. 1, pp. 1290–1303, Dec. 2021. doi:10.1021/acsami.1c09451

[26] Mao, S.S. *et al.*, “Dynamics of femtosecond laser interactions with dielectrics” *Applied Physics A* 79, 1695–1709 June. 2004.

[27] Eaton, S. M. *et al.*, “Transition from thermal diffusion to heat accumulation in high repetition rate femtosecond laser writing of buried optical waveguides” *Opt. Express* 16(13), 9443-9458 Dec. 2008.

[28] F. R. Wagner, C. Gouldieff, J.-Y. Natoli, and M. Commandré, “Nanosecond multi-pulse laser-induced damage mechanisms in pure and mixed oxide thin films,” *Thin Solid Films*, vol. 592, pp. 225–231, Oct. 2015. doi:10.1016/j.tsf.2015.04.014

[29] A. Melninkaitis *et al.*, “The effect of pseudo-accumulation in the measurement of fatigue laser-induced damage threshold,” *Laser-Induced Damage in Optical Materials: 2008*, Oct. 2008. doi:10.1117/12.804467

[30] H. Ye, Y. Li, Q. Xu, C. Jiang, and Z. Wang, “Resistance of scratched fused silica surface to UV laser induced damage,” *Scientific Reports*, vol. 9, no. 1, Jul. 2019. doi:10.1038/s41598-019-46048-4

[31] J. Peatross and M. Ware, *Physics of Light and Optics*. Provo, UT: Brigham Young University, Department of Physics, 2023.

[32] Z. Balogh-Michels *et al.*, “Crystallization of HFO2 thin films and their influence on laser induced damage,” *EPJ Web of Conferences*, vol. 238, p. 12004, 2020. doi:10.1051/epjconf/202023812004

[33] S. Zhou *et al.*, “Crystallization of geo2 thin films into α-quartz: From spherulites to single crystals,” *Acta Materialia*, vol. 215, p. 117069, Aug. 2021. doi:10.1016/j.actamat.2021.117069

[34] O. Durante *et al.*, “Emergence and evolution of crystallization in tio2 thin films: A structural and Morphological Study,” *Nanomaterials*, vol. 11, no. 6, p. 1409, May 2021. doi:10.3390/nano11061409

[35] D. Ristau, *Laser-Induced Damage in Optical Materials*. Boca Raton, FL: CRC Press, Taylor & Francis Group, 2015.

[36] L. Sun *et al.*, “Effects of combined process of reactive ion etching and dynamic chemical etching on UV laser damage resistance and surface quality of fused silica optics,” *Optics Express*, vol. 26, no. 14, p. 18006, Jun. 2018. doi:10.1364/oe.26.018006

[37] L. Sun *et al.*, “Combination of reaction ion etching and dynamic chemical etching for improving laser damage resistance of fused silica optical surfaces,” *Optics Letters*, vol. 41, no. 19, p. 4464, Sep. 2016. doi:10.1364/ol.41.004464

[38] B. Li *et al.*, “Layer by layer exposure of subsurface defects and laser-induced

damage mechanism of fused silica," *Applied Surface Science*, vol. 508, p. 145186, Apr. 2020. doi:10.1016/j.apsusc.2019.145186

[39] L. O. Jensen *et al.*, "e;es on SiO2 /HfO2 mixtures for nanosecond and femtosecond pulses," *SPIE Proceedings*, Oct. 2010. doi:10.1117/12.867238

[40] G. Abromavičius, S. Kičas, and R. Buzelis, "High temperature annealing effects on spectral, microstructural and laser damage resistance properties of sputtered HFO2 and HFO2-sio2 mixture-based UV mirrors," *Optical Materials*, vol. 95, p. 109245, Sep. 2019. doi:10.1016/j.optmat.2019.109245

[41] L. Gallais *et al.*, "Laser damage of silica and hafnia thin films made with different deposition technologies," *SPIE Proceedings*, Oct. 2007. doi:10.1117/12.752952

[42] S. Papernov *et al.*, "Optical properties of oxygen vacancies in HfO2 thin films studied by absorption and Luminescence Spectroscopy," *Optics Express*, vol. 26, no. 13, p. 17608, Jun. 2018. doi:10.1364/oe.26.017608

[43] C. Xu *et al.*, "Correlations between the oxygen deficiency and the laser damage resistance of different oxide films," *Applied Surface Science*, vol. 289, pp. 141–144, Jan. 2014. doi:10.1016/j.apsusc.2013.10.121

[44] D. N. Nguyen, L. A. Emmert, D. Patel, C. S. Menoni, and W. Rudolph, "Transient phenomena in the dielectric breakdown of HFO2 optical films probed by Ultrafast Laser Pulse pairs," *Applied Physics Letters*, vol. 97, no. 19, Nov. 2010. doi:10.1063/1.3511286

[45] C. R. Wolfe, "Laser conditioning of optical thin films," *Laser-Induced Damage in Optical Materials 1989*, Nov. 1990. doi:10.1117/12.2294445

[46] R. Pakalnyte, E. Pupka, and A. Melninkaitis, "Direct comparison of laser-induced damage threshold testing protocols on dielectric mirrors: Effect of nanosecond laser pulse shape at NIR and UV wavelengths," *Laser-induced Damage in Optical Materials 2019*, Dec. 2019. doi:10.1117/12.2536456

[47] T. Willemsen *et al.*, "Large area ion beam sputtered dielectric ultrafast mirrors for petawatt laser beamlines," *Optics Express*, vol. 30, no. 4, p. 6129, Feb. 2022. doi:10.1364/oe.452249

[48] Y. Zhao, T. Wang, D. Zhang, J. Shao, and Z. Fan, "Laser conditioning and multi-shot laser damage accumulation effects of HFO2/sio2 antireflective coatings," *Applied Surface Science*, vol. 245, no. 1–4, pp. 335–339, May 2005. doi:10.1016/j.apsusc.2004.10.028

[49] M. R. Kozlowski, "Large area laser conditioning of dielectiic thin film mirrors," *Laser-Induced Damage in Optical Materials 1989*, Nov. 1990. doi:10.1117/12.2294446

[50] J. Hu, X. Zhou, F. Pan, and Q. Xu, "Effect of laser conditioning on nanoprecursor for improving laser damage resistance of HFO2coatings," *Laser Physics*, vol. 28, no. 3, p. 036003, Feb. 2018. doi:10.1088/1555-6611/aa9d08

[51] N. Bartels, P. Allenspacher, and W. Riede, “Laser conditioning of UV anti-reflective optical coatings for applications in Aerospace,” *Laser-Induced Damage in Optical Materials 2018: 50th Anniversary Conference*, Nov. 2018. doi:10.1117/12.2326782

[52] C. J. Stolz *et al.*, “Laser conditioning methods of Hafnia silica multilayer mirrors,” *SPIE Proceedings*, Jun. 1998. doi:10.1117/12.311905

[53] C. J. Stolz, L. M. Sheehan, S. M. Maricle, S. Schwartz, and J. Hue, “Laser conditioning methods of Hafnia-silica multilayer mirrors,” *SPIE Proceedings*, Apr. 1999. doi:10.1117/12.344419

[54] F. Dai, W. Shi, B. Yang, and W. Huang, “Study on laser conditioning parameters of HfO2 SiO2 Multilayer mirrors,” *Advances in Materials Physics and Chemistry*, vol. 07, no. 06, pp. 242–254, 2017. doi:10.4236/ampc.2017.76019

[55] A. B. Papandrew, C. J. Stolz, Z. Wu, G. E. Loomis, and S. Falabella, “Laser conditioning characterization and damage threshold prediction of Hafnia/silica multilayer mirrors by photothermal microscopy,” *Laser-Induced Damage in Optical Materials: 2000*, Apr. 2001. doi:10.1117/12.425049

[56] F. Bonneau *et al.*, “Study of UV laser interaction with gold nanoparticles embedded in silica,” *Applied Physics B: Lasers and Optics*, vol. 75, no. 8, pp. 803–815, Dec. 2002. doi:10.1007/s00340-002-1049-7

[57] J. W. Pinder *et al.*, “Avoiding common errors in X-ray photoelectron spectroscopy data collection and analysis, and properly reporting instrument parameters,” *Applied Surface Science Advances*, vol. 19, p. 100534, Feb. 2024. doi:10.1016/j.apsadv.2023.100534

[58] G. H. Major *et al.*, “Practical guide for curve fitting in x-ray photoelectron spectroscopy,” *Journal of Vacuum Science & Technology A*, vol. 38, no. 6, p. 061203, Dec. 2020, doi: https://doi.org/10.1116/6.0000377.

[59] G. Greczynski and L. Hultman, “X-ray photoelectron spectroscopy: Towards reliable binding energy referencing,” *Progress in Materials Science*, vol. 107, p. 100591, Jan. 2020. doi:10.1016/j.pmatsci.2019.100591

[60] H. Wang *et al.*, “Study of reactions between HFO2 and si in thin films with precise identification of chemical states by XPS,” *Applied Surface Science*, vol. 257, no. 8, pp. 3440–3445, Feb. 2011. doi:10.1016/j.apsusc.2010.11.042

[61] J. Liu, R. M. Martin, and J. P. Chang, “Characteristics of HF-silicate thin films synthesized by plasma enhanced atomic layer deposition,” *Journal of Vacuum Science & Technology A: Vacuum, Surfaces, and Films*, vol. 26, no. 5, pp. 1251–1257, Aug. 2008. doi:10.1116/1.2966430

[62] M.-H. Cho, K. B. Chung, C. N. Whang, D. W. Lee, and D.-H. Ko, “Phase separation and electronic structure of HF-silicate film as a function of composition,” *Applied Physics Letters*, vol. 87, no. 24, Dec. 2005. doi:10.1063/1.2143132

[63] K. Yan *et al.*, “Oxygen vacancy induced structure change and interface reaction in

HFO2 films on native sio2/si substrate," *Applied Surface Science*, vol. 390, pp. 260–265, Dec. 2016. doi:10.1016/j.apsusc.2016.08.051

[64] G. He, M. Liu, L. Q. Zhu, M. Chang, Q. Fang, and L. D. Zhang, "Effect of postdeposition annealing on the thermal stability and structural characteristics of sputtered HfO2 films on Si (100)," *Surface Science*, vol. 576, no. 1–3, pp. 67–75, Feb. 2005, doi: https://doi.org/10.1016/j.susc.2004.11.042.

[65] M. C. Biesinger, "Accessing the robustness of adventitious carbon for charge referencing (correction) purposes in XPS analysis: Insights from a multi-user facility data review," *Applied Surface Science*, vol. 597, p. 153681, Sep. 2022, doi: https://doi.org/10.1016/j.apsusc.2022.153681.

[66] W. Liu, P. Yang, B. Qin, Y. Cao, J. Zhang, and D. Zhu, "Investigations on single and multiple pulse laser-induced damages in Al2O3/SiO2 multilayer dielectric films at 355 nm," *Optical Engineering*, vol. 57, no. 12, p. 1, Sep. 2018, doi: https://doi.org/10.1117/1.oe.57.12.121905.

[67] J. A. Folta *et al.*, "Mitigation of Laser Damage on NIF Optics in Volume Production," Nov. 2013.

[68] M. L. Spaeth *et al.*, "Optics Recycle Loop Strategy for NIF Operations above UV Laser-Induced Damage Threshold," *Fusion Science and Technology*, vol. 69, no. 1, pp. 265–294, Feb. 2016, doi: https://doi.org/10.13182/fst15-119.

[69] L. M. Kegelmeyer et al., "Automated optics inspection analysis for NIF," Fusion Engineering and Design, vol. 87, no. 12, pp. 2120–2124, Dec. 2012, doi: https://doi.org/10.1016/j.fusengdes.2012.09.017

[70] T. Tabata, Sebastien Halty, Fabien Rozé, K. Huet, and F. Mazzamuto, "Non-doped HfO2 crystallization controlled by dwell time in laser annealing," Applied Physics Express, vol. 14, no. 11, pp. 115503–115503, Oct. 2021, doi: https://doi.org/10.35848/1882-0786/ac2c18.

[71] J. R. Palmer, "Continuous Wave Laser Damage On Optical Components," Optical Engineering, vol. 22, no. 4, Aug. 1983, doi: https://doi.org/10.1117/12.7973140.

[72] J. Taniguchi et al., "Functional damage thresholds of hafnia/silica coating designs for the NIF laser," Proceedings of SPIE, the International Society for Optical Engineering/Proceedings of SPIE, Apr. 2001, doi: https://doi.org/10.1117/12.425071.

[73] A. A. Manenkov, "Fundamental mechanisms of laser-induced damage in optical materials: today's state of understanding and problems," Optical Engineering, vol. 53, no. 1, pp. 010901–010901, Jan. 2014, doi: https://doi.org/10.1117/1.oe.53.1.010901.

[74] S. Papernov and A. W. Schmid, "Localized absorption effects during 351 nm, pulsed laser irradiation of dielectric multilayer thin films," Journal of Applied Physics, vol. 82, no. 11, pp. 5422–5432, Dec. 1997, doi: https://doi.org/10.1063/1.365570.

[75] S. V Popruzhenko, “Keldysh theory of strong field ionization: history, applications, difficulties and perspectives,” Journal of Physics B: Atomic, Molecular and Optical Physics, vol. 47, no. 20, p. 204001, Oct. 2014, doi: https://doi.org/10.1088/0953-4075/47/20/204001.

[76] H. Chen and W. Z. Shen, “Perspectives in the characteristics and applications of Tauc-Lorentz dielectric function model,” The European Physical Journal B, vol. 43, no. 4, pp. 503–507, Feb. 2005, doi: https://doi.org/10.1140/epjb/e2005-00083-9.

[77] D. Schwarz, H. Wormeester, and B. Poelsema, “Validity of Lorentz–Lorenz equation in porosimetry studies,” Thin Solid Films, vol. 519, no. 9, pp. 2994–2997, Feb. 2011, doi: https://doi.org/10.1016/j.tsf.2010.12.053.

[78] E. Tuncer, Y. V. Serdyuk, and S. M. Gubanski, “Dielectric mixtures: electrical properties and modeling,” IEEE Transactions on Dielectrics and Electrical Insulation, vol. 9, no. 5, pp. 809–828, Oct. 2002, doi: https://doi.org/10.1109/tdei.2002.1038664.

[79] C. J. Stolz and R. A. Negres, “Ten-year summary of the Boulder Damage Symposium annual thin film laser damage competition,” Optical Engineering, vol. 57, no. 12, p. 1, Dec. 2018, doi: https://doi.org/10.1117/1.oe.57.12.121910.

[80] A. Zaccone, Theory of Disordered Solids. Springer Nature, 2023.

[81] S. M. Sze and K. K. Ng, PHYSICS OF SEMICONDUCTOR DEVICES, 3RD ED. John Wiley & Sons, 2008.

[82] M. H. Cohen, “Review of the theory of amorphous semiconductors,” Journal of Non-crystalline Solids, vol. 4, pp. 391–409, Apr. 1970, doi: https://doi.org/10.1016/0022-3093(70)90068-2.

[83] L. Yang, G. Vajente, M. Fazio, A. Ananyeva, G. Billingsley, A. Markosyan, R. Bassiri, K. Prasai, M. M. Fejer, and C. S. Menoni, Enhanced medium-range order in vapor-deposited germania glasses at elevated temperatures, Sci. Adv. 7, eabh1117 (2021).

[84] Agata Obstarczyk et al., “The effect of post-process annealing on optical and electrical properties of mixed HfO2–TiO2 thin film coatings,” Journal of Materials Science Materials in Electronics, vol. 30, no. 7, pp. 6358–6369, Feb. 2019, doi: https://doi.org/10.1007/s10854-019-00938-5.

[85] V. V. Zhurin, H. R. Kaufman, J. R. Kahn, and T. L. Hylton, “Biased target deposition,” Journal of Vacuum Science & Technology A Vacuum Surfaces and Films, vol. 18, no. 1, pp. 37–41, Jan. 2000, doi: https://doi.org/10.1116/1.582155.

[86] A. Anders, “A structure zone diagram including plasma-based deposition and ion etching,” Thin Solid Films, vol. 518, no. 15, pp. 4087–4090, May 2010, doi: https://doi.org/10.1016/j.tsf.2009.10.145.

[87] M. Ohring, The materials science of thin films. San Diego, Calif. ; London:

Academic, 2002.

[88] M. Mende, L. O. Jensen, H. Ehlers, W. Riggers, H. Blaschke, and D. Ristau, “Laser-induced damage of pure and mixture material high reflectors for 355nm and 1064nm wavelength,” Proceedings of SPIE, the International Society for Optical Engineering/Proceedings of SPIE, Sep. 2011, doi: https://doi.org/10.1117/12.897049.

[89] R. A. Negres, C. J. Stolz, M. D. Thomas, and M. Caputo, “355-nm, nanosecond laser mirror thin film damage competition,” OSTI OAI (U.S. Department of Energy Office of Scientific and Technical Information), Nov. 2017, doi: https://doi.org/10.1117/12.2279981.

[90] M. A. Fazio, A. Ananjeva, G. Vajente, L. Yang, and C. S. Menoni, “Elastic properties of amorphous thin film oxides,” 2022 IEEE Photonics Conference (IPC), Nov. 2022, doi: https://doi.org/10.1109/ipc53466.2022.9975614.

[91] A. Davenport et al., “The Development of High Reflection TiO2:GeO2 and SiO2 Coatings for Gravitational Wave Detectors,” Optical Interference Coatings Conference (OIC) 2022, Jan. 2022, doi: https://doi.org/10.1364/oic.2022.wa.6.

[92] M. Mende, S. Schrameyer, H. Ehlers, D. Ristau, and L. Gallais, “Laser damage resistance of ion-beam sputtered Sc2O3/SiO2 mixture optical coatings,” Applied Optics, vol. 52, no. 7, p. 1368, Feb. 2013, doi: https://doi.org/10.1364/ao.52.001368.

[93] M. J. Runkel, K. P. Neeb, M. C. Staggs, J. Auerbach, and A. K. Burnham, “Results of raster-scan laser conditioning studies on DKDP triplers using Nd:YAG and excimer lasers,” Proceedings of SPIE, the International Society for Optical Engineering/Proceedings of SPIE, Mar. 2002, doi: https://doi.org/10.1117/12.461713.

[94] Andrius Melninkaitis et al., “Recent advancements in standardization effort for laser-induced damage threshold testing,” Jun. 2024, doi: https://doi.org/10.1117/12.3023107.

[95] G. Batavičiutė, P. Grigas, L. Smalakys, and A. Melninkaitis, “Revision of laser-induced damage threshold evaluation from damage probability data,” Review of Scientific Instruments, vol. 84, no. 4, p. 045108, Apr. 2013, doi: https://doi.org/10.1063/1.4801955.

[96] L. B. Jonsson, T. Nyberg, I. Katardjiev, and S. Berg, “Frequency response in pulsed DC reactive sputtering processes,” Thin Solid Films, vol. 365, no. 1, pp. 43–48, Apr. 2000, doi: https://doi.org/10.1016/s0040-6090(99)01116-5.

[97]P. B. Mirkarimi et al., “Improving the laser performance of ion beam sputtered dielectric thin films through the suppression of nanoscale defects by employing a xenon sputtering gas,” Optical Materials Express, vol. 12, no. 9, pp. 3365–3365, Aug. 2022, doi: https://doi.org/10.1364/ome.462407.

[98] M. D. Feit and A. M. Rubenchik, “Implications of nanoabsorber initiators for damage probability curves, pulselength scaling, and laser conditioning,” Jun. 2004, doi: https://doi.org/10.1117/12.523862.

[99] West, K. G.; Lu, J.; Yu, J.; Kirkwood, D.; Chen, W.; Pei, Y.; Claassen, J.; Wolf, S. A. Growth and Characterization of Vanadium Dioxide Thin Films Prepared by Reactive-Biased Target Ion Beam Deposition. Journal of Vacuum Science & Technology A: Vacuum, Surfaces, and Films 2008, 26 (1), 133–139. https://doi.org/10.1116/1.2819268.

[100] X. Fu, M. Commandre, Laurent Gallais, M. Mende, H. Ehlers, and D. Ristau, “Laser-induced damage in composites of scandium, hafnium, aluminum oxides with silicon oxide in the infrared,” Applied Optics, vol. 53, no. 4, pp. A392–A392, Jan. 2014, doi: https://doi.org/10.1364/ao.53.00a392.

[101] T. V. Amotchkina, M. K. Trubetskov, Vladimir Pervak, et al “On the reliability of reverse engineering results,” Applied Optics, vol. 51, no. 22, pp. 5543–5543, Jul. 2012, doi: https://doi.org/10.1364/ao.51.005543.

[102] H. Kaufman and R. Robinson, “End-Hall ion source,” Oct. 20, 1986 Available: https://patents.google.com/patent/US4862032A/en

[103] X. Fu et al., “Investigation of the distribution of laser damage precursors at 1064 nm, 12 ns on Niobia-Silica and Zirconia-Silica mixtures,” Optics Express, vol. 20, no. 23, pp. 26089–26089, Nov. 2012, doi: https://doi.org/10.1364/oe.20.026089.

[104] C. W. Carr, H. B. Radousky, A. M. Rubenchik, M. D. Feit, and S. G. Demos, “Localized dynamics during laser-induced damage in optical materials,” Physical Review Letters, vol. 92, no. 8, p. 087401, Feb. 2004, doi: https://doi.org/10.1103/PhysRevLett.92.087401.

[105] M. Fazio et al., “Structure and morphology of low mechanical loss TiO2-doped Ta2O5,” Optical Materials Express, vol. 10, no. 7, pp. 1687–1687, Jun. 2020, doi: https://doi.org/10.1364/ome.395503.

[106] A. B. Zylstra et al., “Burning plasma achieved in inertial fusion,” Nature, vol. 601, no. 7894, pp. 542–548, Jan. 2022, doi: https://doi.org/10.1038/s41586-021-04281-w.

[107] D. L. Wood, K. Nassau, T. Y. Kometani, and D. L. Nash, “Optical properties of cubic hafnia stabilized with yttria,” Applied Optics, vol. 29, no. 4, pp. 604–604, Feb. 1990, doi: https://doi.org/10.1364/ao.29.000604.

[108] H. Bach and D. Krause, Thin Films on Glass. Springer Science & Business Media, 2013, pp. 162–165.

[109] L. V. Rodríguez-de and J. I. Larruquert, “Analytic optical-constant model derived from Tauc-Lorentz and Urbach tail,” Optics Express, vol. 24, no. 25, pp. 28561–28561, Dec. 2016, doi: https://doi.org/10.1364/oe.24.028561.

[110] M. Fazio et al., “Structure and morphology of low mechanical loss TiO2-doped Ta2O5,” Optical Materials Express, vol. 10, no. 7, pp. 1687–1687, Jun. 2020, doi: https://doi.org/10.1364/ome.395503.

[111] C. Spinella, S. Lombardo, and F. Priolo, “Crystal grain nucleation in amorphous silicon,” Journal of Applied Physics, vol. 84, no. 10, pp. 5383–5414, Nov. 1998, doi: https://doi.org/10.1063/1.368873.

[112] T.-J. Chen and C.-L. Kuo, “First principles study of the structural, electronic, and dielectric properties of amorphous HfO2,” Journal of Applied Physics, vol. 110, no. 6, Sep. 2011, doi: https://doi.org/10.1063/1.3636362.

[113] J. C. Hackley and T. Gougousi, “Properties of atomic layer deposited HfO2 thin films,” Thin Solid Films, vol. 517, no. 24, pp. 6576–6583, Oct. 2009, doi: https://doi.org/10.1016/j.tsf.2009.04.033.

[114] P. Chu, Advances in Solid State Circuit Technologies. BoD – Books on Demand, 2010.

[115] E. Hecht and Pearson Education, Optics, 5th ed. Boston Etc.: Pearson, Cop, 2017.

[116] J. H. Apfel, “Optical coating design with reduced electric field intensity,” Applied Optics, vol. 16, no. 7, pp. 1880–1880, Jul. 1977, doi: https://doi.org/10.1364/ao.16.001880.

[117] S. Fan et al., “Vibrational fingerprints of ferroelectric HfO2,” npj Quantum Materials, vol. 7, no. 1, Mar. 2022, doi: https://doi.org/10.1038/s41535-022-00436-8.

[118] M. Zhu et al., “Research on the laser damage performance of high reflection coatings at 355 nm,” Proceedings of SPIE, the International Society for Optical Engineering/Proceedings of SPIE, Jul. 2013, doi: https://doi.org/10.1117/12.2020859.

[119] G. Vajente et al., “Low Mechanical Loss TiO2:GeO2 Coatings for Reduced Thermal Noise in Gravitational Wave Interferometers,” Physical Review Letters, vol. 127, no. 7, Aug. 2021, doi: https://doi.org/10.1103/physrevlett.127.071101.

[120] P. Mulser, “Inertial confinement fusion with lasers or particle beams,” Plasma Physics and Controlled Fusion, vol. 28, no. 1A, pp. 203–218, Jan. 1986, doi: https://doi.org/10.1088/0741-3335/28/1a/018.

[121] Nuckolls, J. et al. Laser compression of matter to super-high densities: thermonuclear (CTR) applications. Nature 239, 139–142 (1972).

[122] J. D. Lawson, “Some Criteria for a Power Producing Thermonuclear Reactor,” Proceedings of the Physical Society. Section B, vol. 70, no. 1, pp. 6–10, Jan. 1957, doi: https://doi.org/10.1088/0370-1301/70/1/303.

[123] G. Abromavičius, T. Juodagalvis, R. Buzelis, K. Juškevičius, R. Drazdys, and S. Kičas, “Oxygen plasma etching of fused silica substrates for high power laser optics,” Applied Surface Science, vol. 453, pp. 477–481, Sep. 2018, doi: https://doi.org/10.1016/j.apsusc.2018.05.105.

[124] Y. A. Kutoyants, Introduction to the Statistics of Poisson Processes and Applications. Springer Nature

[125] A. S. Thill et al., “Shifting the band gap from UV to visible region in cerium oxide nanoparticles,” Applied Surface Science, vol. 528, p. 146860, Oct. 2020, doi: https://doi.org/10.1016/j.apsusc.2020.146860.

[126] F. Shi, Y. Zhong, Y. Dai, X. Peng, M. Xu, and T. Sui, “Investigation of surface damage precursor evolutions and laser-induced damage threshold improvement mechanism during Ion beam etching of fused silica,” Optics Express, vol. 24, no. 18, p. 20842, Aug. 2016, doi: https://doi.org/10.1364/oe.24.020842.

[127] L. O. Jensen and D. Ristau, “Coatings of oxide composites,” SPIE Proceedings, vol. 8530, p. 853013, Dec. 2012, doi: https://doi.org/10.1117/12.981526.

[128] N. D. Browning, D. J. Wallis, P. D. Nellist, and S. J. Pennycook, “EELS in the STEM: Determination of materials properties on the atomic scale,” *Micron*, vol. 28, no. 5, pp. 333–348, Oct. 1997, doi: https://doi.org/10.1016/s0968-4328(97)00033-4.

[129] J. M. Sanz, M. A. Bañon, E. Elizalda, and F. Yubero, “An interpretation of the electron energy loss spectra of clean and oxygen exposed hafnium,” *Journal of Electron Spectroscopy and Related Phenomena*, vol. 48, no. 1, pp. 143–153, Jan. 1989, doi: https://doi.org/10.1016/0368-2048(89)80012-x

[130] M.L. Spaeth et al, Description of the NIF laser, Fusion Science and Technology 69, 25-145 (2016).

[131] T.R. Boehly, et al, , Inertial confinement fusion experiments with OMEGA-A 30-kJ, 60-beam UV laser. Fusion Engineering and Design, 44: p. 35-42, (1999).

[132] J. F. Holzrichter, E. M. Campbell, J. D. Lindl, and E. Storm, “Research with High-Power Short-Wavelength Lasers,” Science, vol. 229, no. 4718, pp. 1045–1051, Sep. 1985, doi: https://doi.org/10.1126/science.229.4718.1045.

Appendix - Supplementary Materials

5.1 Optical properties of biased target deposition antireflection coatings for λ=355 nm

The biased target deposited (BTD anti-reflection (AR) coatings for λ=355 nm consists of two layers, the high index layer deposited on the substrate and a next layer of SiO2, the low index layer in the coating. The normalized electric field intensity, $\left|\frac{E^2}{E_{inc}^2}\right|$, in the two-layer ARs is shown in Fig. S1(a). The normalized electric field intensity peaks at a value of 66% at the substrate/high index layer interface. The field intensity at the SiO_2-Air interface is larger than at the substrate/high index layer interface but the laser induced damage threshold of SiO_2 is higher than the high index layer, so laser damage is not expected to occur in this layer. The transmission at λ=355nm is ~96%, which is an improvement from the 92.9% of the substrate. If the AR coating were deposited on the backside of the substrate, which is typically the case in AR coatings used in applications, the transmission would increase to ~99% as shown in Fig S1b.

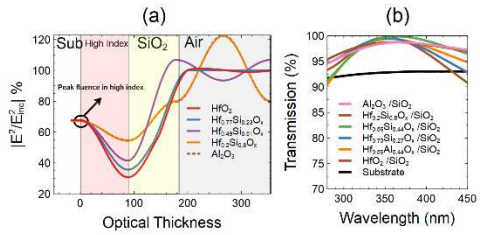

Fig. S1. (a) Electric field distribution in two-layer anti-reflection coatings from Table 1. (b) Transmission of AR coatings at 355nm.

5.2 Calculation of the degree of porosity from the dispersion of the refractive index

It has previously been shown that the porosity of mixture amorphous oxide alloys can be obtained from the analysis of the dispersion of the refractive index [1,2]. This approach uses the Lorentz-Lorenz effective medium approximation (LL EMA) to establish the relationship between index of refraction and mixture percentage. The form

of the LL EMA is shown in Eq. (S1). Using this EMA porosity, the volume fraction of voids can be calculated using Eq. (S2) [3]:

$$\frac{(n_{eff}^2-1)}{(n_{eff}^2+2)} = f_1 \frac{(n_1^2-1)}{(n_1^2+2)} + f_2 \frac{(n_2^2-1)}{(n_2^2+2)} \quad \text{(S1)}$$

$$P(\%) = \left[1 - \frac{(n_{eff}^2-1)}{(n_{bulk}^2+2)}\right] * 100 \quad \text{(S2)}$$

Where n_{eff} is the measured index of refraction, n_{bulk} is the index of refraction of the bulk materials at 1µm (HfO_2 =2.11 [4], SiO_2 =1.54 [5]), n_1 is the refractive index of hafnia, n_2 is the refractive index of the dopant, and f_1/f_2 is the volume fraction of hafnia and the dopant respectively. The complex index of refraction is first extracted from ellipsometry (HORIBA UVISEL) data fitting with a 3-oscillator Tauc Lorentz model [4]. The transmission spectrum from 190-1300nm is measured at 0-degree angle of incidence using a PerkinElmer LAMBDA 1050 spectrophotometer. The index is further refined by reverse engineering the transmission spectrum using OptiRE™.

5.3 Structural properties of BTD amorphous oxide thin films

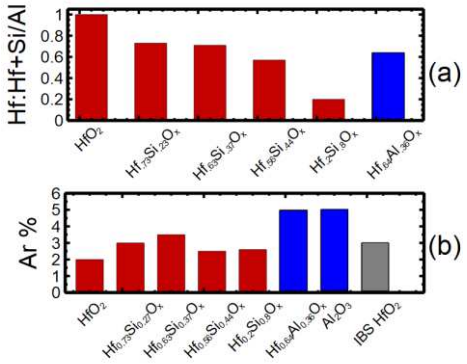

Fig. S2. (a) Atomic ratio of Hf to (Hf+Si/Al) as determined by RBS in red and prediction of the LL EMA from the measured refractive index in blue,(b) Measured argon concentration in high index materials

Rutherford backscattering spectrometry (RBS) was performed using He^+ ions at 2.035 MeV with a 1.7 MV Tandetron accelerator. Spectra were acquired with samples tilted at 7◦. The scattered ions were collected at an angle of 10◦ from the beam. The experimental spectra were simulated using the SIMNRA software to extract the composition and atomic density of the deposited layers [7].

RBS results also provide the surface density of the thin films which in combination with the layer thickness allows one to calculate the volumetric density tabulated in Table S1 for all samples used in this study. X-ray photoelectron spectroscopy was used to assess the bonding in the HfO_2 mixtures. For these measurements the thin film materials were sputtered onto highly doped silicon wafers to prevent charging effects during measurement. High resolution spectra of the Hf 4f, Si 2p, and O 1s orbitals were measured. XPS spectra was collected using the Physical Electronics PE 5800 ESCA/ASE spectrometer with monochromatic Al Kα X-rays (1486.6 eV) and a take-off angle of 45°. A charge neutralizer was used during measurement. The base pressure was 1×10^{-9} Torr, and 1×10^{-8} Torr during measurement. Analysis was assisted by CasaXPS software.

Table S1: RBS results of atomic density in the materials used in the optical coatings

Fabrication Method/Material	Volumetric Atomic Density (atoms/cm^3)
BTD $Hf_{0.64}Al_{0.36}O_x$	7.95E+22
BTD $Hf_{0.2}Si_{0.8}O_x$	6.99E+22
BTD $Hf_{0.56}Si_{0.44}O_x$	7.62E+22
BTD $Hf_{0.63}Si_{0.37}O_x$	7.83E+22
BTD $Hf_{0.73}Si_{0.27}O_x$	8.21E+22
BTD HfO_2	6.67E+22
BTD SiO_2	4.12E+22
BTD Al_2O_3	9.52E+22
IBS HfO_2	8.74E+22
IBS SiO_2	4.64E+22
EBE HfO_2	4.78E+22
EBE SiO_2	3.89E+22

Binding energy calibration was performed by deconvolving the C 1s peak with the C-C component attuned to the well-known energy of 248.8eV [5]. XPS spectra from SiO_2, HfO_2 and mixtures of $Hf_{0.56}Si_{0.44}O_x$ and $Hf_{0.2}Si_{0.8}O_x$ are shown in Fig. S3. The XPS measurements in Fig. 3(a-d) show the deconvolved high resolution spectra for the Si 2p, O 1s, and Hf 4f orbitals. The FWHM of the O 1s emission increases significantly in the mixture materials indicating the presence of a new bonding type, Hf-O-Si, which has a binding energy less than O-Si-O, but greater than O-Hf-O [6]. In agreement with XPS studies on hafnium silicate, the O 1s binding energy position shifts linearly with mixture concentration [7-9]. This implies increasing contribution of Si bonds and decreasing contribution of Hf bonds with increasing Si concentration. These results confirm that these materials are not a true chemical composite, but a collection of pure and mixed chemical states throughout the film.

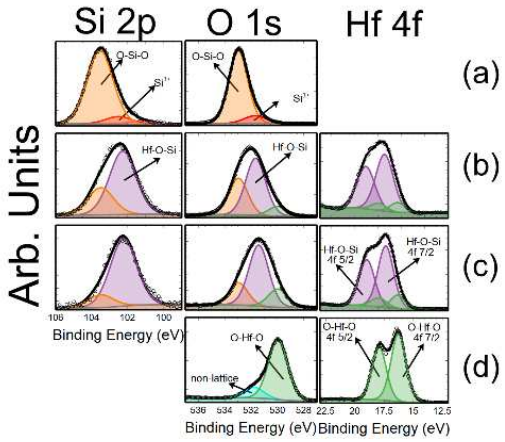

Fig S3 - High resolution XPS spectra of the Si 2p, O 1s, and Hf 4f emission for (a) SiO_2, (b) $Hf_{0.56}Si_{0.44}O_x$, (c) $Hf_{0.2}Si_{0.8}O_x$ and (d) HfO_2. Purple, green, and orange represent Hf-O-Si, O-Hf-O, and O-Si-O bonds respectively.

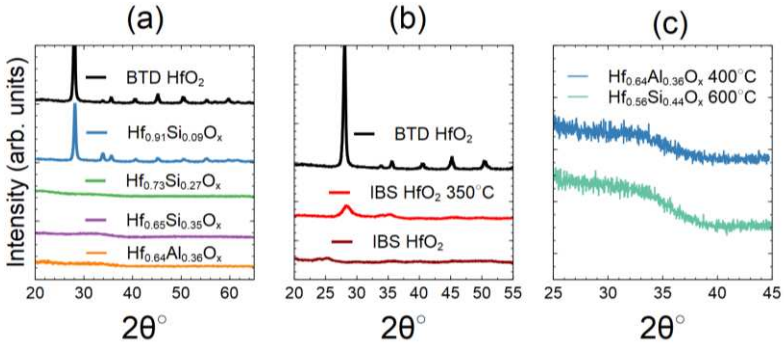

Fig S.4 (a) GI-XRD measurements depict the suppressed crystallization of HfO_2 when SiO_2 or Al_2O_3 concentration exceeds ~10%. (b) Crystallographic structure of HfO_2 fabricated by BTD and IBS sputtering methods. (c) Increased crystallization temperature of HfO_2 based mixtures (>=600˚C) over HfO_2 (<=350˚C)

The degree of crystallization of the amorphous single layers of the high index material in the BTD ARs was investigated by Glancing Incidence X-Ray Diffraction (GI-XRD). The system used was a Bruker D8 Series II which is equipped with Cu K-α x-ray source (1.54 Å). A 0.6mm source slit was utilized. Two theta detector scan was performed from 20° to 65°. To minimize the contribution of the substrate an amorphous UVFS substrate was chosen. In conjunction with the choice of substrate, the angle of incidence of x-rays was fixed a glancing angle of 0.8°.

GI-XRD results reveal that HfO_2 fabricated by BTD is polycrystalline while IBS HfO_2 is amorphous unless annealed at 350˚C or higher. This explains the difference in

refractive index between BTD and IBS HfO_2, where polycrystalline material is denser (2.1 vs 2.04 at λ=1μm). As predicted by the theory of crystallization of HfO_2 at low temperature and pressure, the crystalline phase is monoclinic [10]. The crystallization behavior of various mixture concentrations is shown in Fig S4a. $HfSiO_x$ and $HfAlO_x$ data shown confirm that incorporating SiO_2 or Al_2O_3 above ~10% suppresses the crystallization of HfO_2. Mixtures with higher silica content are not shown but are also amorphous as deposited. Al_2O_3 is amorphous as deposited. Another beneficial characteristic of mixtures is the increase in crystallization temperature shown in Fig. S3c. In the case of optical coatings for high LIDT, higher temperature annealing is associated with more complete oxidation of sub-stoichiometric metal atoms [6]. Literature has demonstrated the crystallization temperature of $Hf_{0.2}Si_{0.8}O_x$ and $Hf_{0.46}Si_{0.54}O_x$ were 900˚C and 1000˚C respectively; and when annealed to these temperatures was the UV, ns laser damage increased >2x from the as deposited [11].

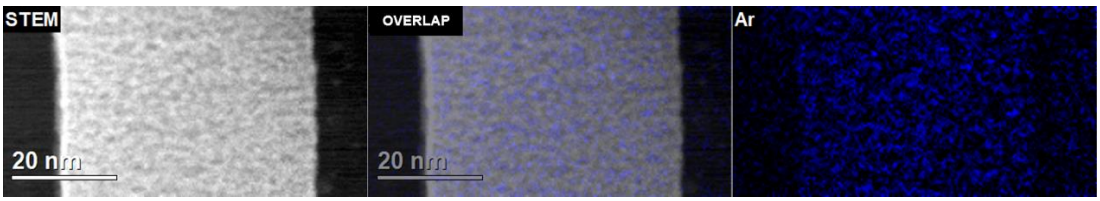

Fig. S5 STEM HAADF image of $Hf_{0.56}Si_{0.44}O_x$ (left), EELS Ar scan (right), Overlap of the HAADF image and Ar concentration (middle)

Scanning Transmission Electron Microscopy with Electron Energy Loss Spectroscopy (STEM-EELS) measurements were performed by Eurofins Materials Science. The $Hf_{0.56}Si_{0.44}O_x$ /SiO_2 AR was prepared with focus ion beam using an FEI Helios Dual Beam system and was thinned to electron transparency. Data were acquired with FEI Titan S/TEM system with accelerator at 200kV in a bright field (BF) and high-angle annular dark-field (HAADF) mode. Figure S5 shows the STEM-HAADF image of the $Hf_{0.56}Si_{0.44}O_x$ overlapped with the EELS scan for Argon. Careful observation shows

the dark regions can be associated with voids or bubbles containing Ar and Oxygen (not shown) in the STEM image overlap with the regions of high Argon concentrations.

5.4 Results of laser damage of BTD and IBS ARs with UV conditioning

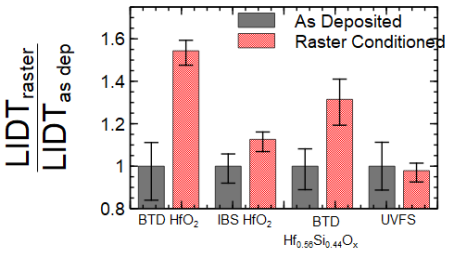

Fig S6.) LIDT of HfO2 coatings deposited by BTD and IBS vs raster scan laser conditioning. Substrate conditioning with no coating is included.

In Fig. S6 the ratio of UV conditioned to unconditioned 1-on-1 LIDT was calculated to illustrate a change in damage threshold due to conditioning. The as-deposited ratio, always equal to 1, is included to show the error bars of the unconditioned and conditioned LIDT. The 1.5x increase in BTD HfO2 is a significant improvement. This increase in the porous BTD ARs is less than that reported in e-beam coatings which can improve by a factor of ~2-3x [12-15] with UV conditioning. Meanwhile, in dense IBS films the impact of laser conditioning is only 11%.

5.5 Morphology of damage in 1-on-1 laser damage tests

The damage morphology in 1-on-1 laser damage tests versus fluence is shown in Fig S7. These images were obtained *ex-situ* with a 40x magnification Nomarski microscope. The top row corresponds to images from the $Hf_{0.2}Si_{0.8}O_x$, AR, the middle row corresponds to images from HfO_2 AR, and the bottom row show catastrophic damage sites from the IBS HR (i) and (ii) and EBE HR. The BTD coatings show microscale (<10 μm) pinhole damage morphology, indicating precursor-initiated damage. Both the IBS and EBE HR have large unconnected craters under the same test site which indicate defect induced damage. Both HR's have also color centers outside of the craters caused by layer delamination or bulging. Unlike the EBE HR, the IBS HR has several microscale

pinholes which are similar to the BTD damage sites, but the size of these pinholes is larger in the IBS case.

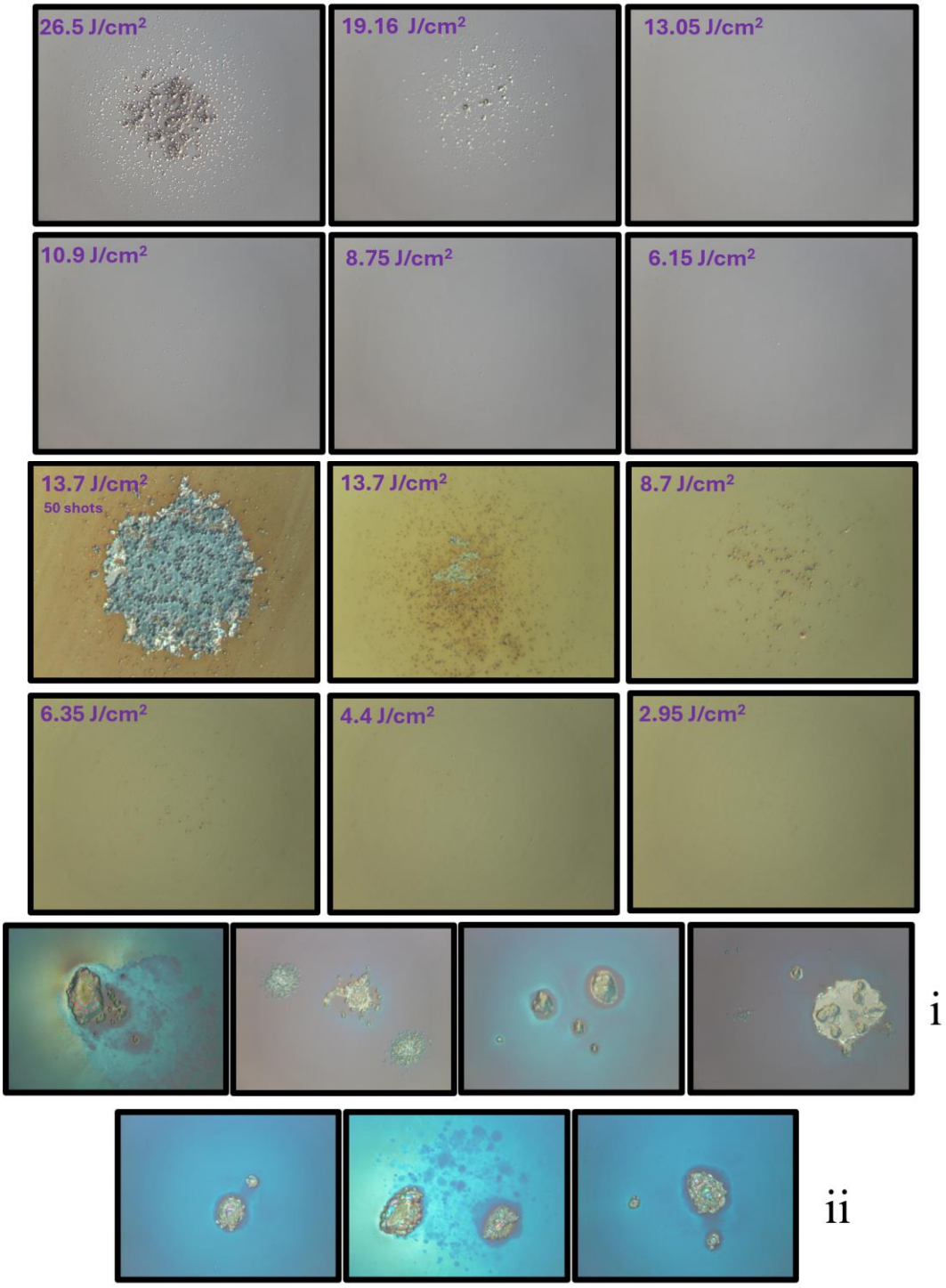

Fig. S7.) Nomarksi microscope images at 40x magnification illustrating the defect-initiated damage morphology of (top) $Hf_{0.2}Si_{0.8}O_x$ 20% Hf mixture AR. (middle) HfO_2/SiO_2 AR at different fluences, (bottom) HfO_2/SiO_2 HRs fabricated by IBS (i) and EBE (ii).

5.6 Supplemental References

[1] D. Schwarz, H. Wormeester, and B. Poelsema, “Validity of Lorentz–Lorenz equation in porosimetry studies,” Thin Solid Films, vol. 519, no. 9, pp. 2994–2997, Feb. 2011, doi: https://doi.org/10.1016/j.tsf.2010.12.053.

[2] E. Tuncer, Y. V. Serdyuk, and S. M. Gubanski, “Dielectric mixtures: electrical properties and modeling,” IEEE Transactions on Dielectrics and Electrical Insulation, vol. 9, no. 5, pp. 809–828, Oct. 2002, doi: https://doi.org/10.1109/tdei.2002.1038664.

[3] M. Mazur, D. Kaczmarek, J. Domaradzki, et al, “Influence of material composition on structural and optical properties of HFO2-TiO2 mixed oxide coatings,” Coatings, vol. 6, no. 1, p. 13, Mar. 2016. doi:10.3390/coatings6010013

[4] D. L. Wood, K. Nassau, T. Y. Kometani, and D. L. Nash, “Optical properties of cubic hafnia stabilized with yttria,” Applied Optics, vol. 29, no. 4, pp. 604–604, Feb. 1990, doi: https://doi.org/10.1364/ao.29.000604.

[5] H. Bach and D. Krause, Thin Films on Glass. Springer Science & Business Media, 2013, pp. 162–165.

[6] H. Chen and W. Z. Shen, “Perspectives in the characteristics and applications of Tauc-Lorentz dielectric function model,” The European Physical Journal B, vol. 43, no. 4, pp. 503–507, Feb. 2005, doi: https://doi.org/10.1140/epjb/e2005-00083-9.

[7] M. Mayer, “SIMNRA, a simulation program for the analysis of NRA, RBS and ERDA,” Jun. 1999, doi: https://doi.org/10.1063/1.59188.

[8] M. C. Biesinger, “Accessing the robustness of adventitious carbon for charge referencing (correction) purposes in XPS analysis: Insights from a multi-user facility data review,” Applied Surface Science, vol. 597, p. 153681, Sep. 2022, doi: https://doi.org/10.1016/j.apsusc.2022.153681.

[9] J. Shi et al., “Effect of annealing on the properties of HFO2-Al2O3 mixture coatings for picosecond laser applications,” Applied Surface Science, vol. 579, p. 152192, Mar. 2022. doi:10.1016/j.apsusc.2021.152192w

[10] H. Wang et al., “Study of reactions between HFO2 and si in thin films with precise identification of chemical states by XPS,” Applied Surface Science, vol. 257, no. 8, pp. 3440–3445, Feb. 2011. doi:10.1016/j.apsusc.2010.11.042

[11] J. Liu, R. M. Martin, and J. P. Chang, “Characteristics of HF-silicate thin films synthesized by plasma enhanced atomic layer deposition,” Journal of Vacuum Science & Technology A: Vacuum, Surfaces, and Films, vol. 26, no. 5, pp. 1251–1257, Aug. 2008. doi:10.1116/1.2966430

[12] M.-H. Cho, K. B. Chung, C. N. Whang, et al, “Phase separation and electronic structure of HF-silicate film as a function of composition,” Applied Physics Letters, vol. 87, no. 24, Dec. 2005. doi:10.1063/1.2143132

[13] N. Kaiser et al., “Defect-stabilized substoichiometric polymorphs of hafnium oxide with semiconducting properties,” ACS Applied Materials & Interfaces, vol. 14, no. 1, pp. 1290–1303, Dec. 2021. doi:10.1021/acsami.1c09451

[14] G. Abromavičius, S. Kičas, and R. Buzelis, “High temperature annealing effects on spectral, microstructural and laser damage resistance properties of sputtered HfO2 and HfO2-SiO2 mixture-based UV mirrors,” Optical Materials, vol. 95, p. 109245, Sep. 2019. doi:10.1016/j.optmat.2019.109245

[15] C. R. Wolfe, “Laser conditioning of optical thin films,” Laser-Induced Damage in Optical Materials 1989, Nov. 1990. doi:10.1117/12.2294445

[16] N. Bartels, P. Allenspacher, and W. Riede, “Laser conditioning of UV anti-reflective optical coatings for applications in Aerospace,” Laser-Induced Damage in Optical Materials 2018: 50th Anniversary Conference, Nov. 2018. doi:10.1117/12.2326782

[17] F. Dai, W. Shi, B. Yang, et al, “Study on laser conditioning parameters of HfO2 SiO2 Multilayer mirrors,” Advances in Materials Physics and Chemistry, vol. 07, no. 06, pp. 242–254, 2017. doi:10.4236/ampc.2017.76019

[18] A. B. Papandrew, C. J. Stolz, Z. Wu, et al, “Laser conditioning characterization and damage threshold prediction of Hafnia/silica multilayer mirrors by photothermal microscopy,” Laser-Induced Damage in Optical Materials: 2000, Apr. 2001. doi:10.1117/12.425049